



OPEN

## Non-linear finite element analysis of SFRC beam-column joints under cyclic loading: enhancing ductility and structural integrity

Umar Ahmad Noor<sup>1</sup>, Muneeb Ahmed Jadoon<sup>1</sup>, Kennedy Onyelowo<sup>2,3</sup>✉, Asif Shahzad<sup>1</sup>, Khaled Ghaedi<sup>4,5</sup>, Hisham Alabduljabbar<sup>6</sup> & Muhammad Faisal Javed<sup>7,8</sup>✉

Brittle shear failure of beam-column joints, especially during seismic events poses a significant threat to structural integrity. This study investigates the potential of steel fiber reinforced concrete (SFRC) in the joint core to enhance ductility and overcome construction challenges associated with traditional reinforcement. A non-linear finite element analysis (NLFEA) using ABAQUS software was conducted to simulate the behavior of SFRC beam-column joints subjected to cyclic loading. Ten simulated specimens were analyzed to discern the impact of varying steel fiber volume fraction and aspect ratio on joint performance. Key findings reveal that a 2% volume fraction of steel fibers in the joint core significantly improves post-cracking behavior by promoting ductile shear failure, thereby increasing joint toughness. While aspect ratio variations showed minimal impact on load capacity, long and thin steel fibers effectively bridge cracks, delaying their propagation. Furthermore, increasing steel fiber content resulted in higher peak-to-peak stiffness. This research suggests that strategically incorporating SFRC in the joint core can promote ductile shear failure, enhance joint toughness, and reduce construction complexities by eliminating the need for congested hoops. Overall, the developed NLFEA model proves to be a valuable tool for investigating design parameters in SFRC beam-column joints under cyclic loading.

**Keywords** Beam-column joint, Ductile shear failure, Steel fiber reinforced concrete, Cyclic loading, Finite element analysis

The beam column connections have been accountable for most structural disasters caused by seismic activity<sup>1</sup>. Due to complex stress state and deficient ductility beam column joints are more exposed to seismic loads in comparison with other structural elements<sup>2-5</sup>. The performance of a frame structure under different loads is heavily impacted by the behavior of its beam-column joints<sup>6</sup>. Furthermore, recent studies inferred that the disfigurement of the beam column connection can cause large story drifts followed by total disintegration of the structures<sup>7-9</sup>. Seismic loads can cause abrupt shear failure of the connection because of the diversified influence of compression, bending, and shear<sup>10-12</sup>. Therefore, drastic disfigurement can occur at beam-column connections due to generation of great forces under seismic activity. Hence, the beam column connection turns out to be one of the most critical sections prone to debacle in framed structures. Unsuitable design and configuration of the reinforcing bars and hoops in beam-column connections is not able to guarantee proper structural ductility<sup>13-15</sup>. Ductility and soundness of the beam-column connections rely on many characteristics such as hoops, rebar's, concrete strength, dimensions of joint and loading conditions etc. To enhance the stability and ductility of Beam-column connection longitudinal and transverse reinforcement is required in the connection. This leads to overcrowding of reinforcement for pouring of concrete and construction snags<sup>16-19</sup>. Across the construction industry, concrete

<sup>1</sup>Department of Civil Engineering, COMSATS University Islamabad, Abbottabad Campus, Abbottabad, Pakistan. <sup>2</sup>Department of Civil Engineering, Michael Okpara University of Agriculture, 440109 UmuDike, Nigeria. <sup>3</sup>Department of Civil Engineering, Kampala International University, Kampala, Uganda. <sup>4</sup>Research and Development Center, PASOFAL Engineering Group, 52200 Kuala Lumpur, Malaysia. <sup>5</sup>Civil Engineering Department, Universiti Putra Malaysia, 43400 Serdang, Selangor, Malaysia. <sup>6</sup>Department of Civil Engineering, College of Engineering in Al-Kharj, Prince Sattam Bin Abdulaziz University, 11942 Al-Kharj, Saudi Arabia. <sup>7</sup>Department of Civil Engineering, Ghulam Ishaq Khan Institute of Engineering Sciences and Technology, Topi, Pakistan. <sup>8</sup>Western Caspian University, Baku, Azerbaijan. ✉email: kennedychibuzor@kiu.ac.ug; arbabfaisal@cuatd.edu.pk

stands out as the most frequently employed material, primarily due to its affordability and ability to have its properties altered to suit a variety of different applications. However, due to its brittle nature conventional concrete has less ductility and energy absorption resulting in a particularly weaker response against certain loading conditions including seismic loading<sup>20–22</sup>. Different additives or components can be used to alter the properties of a concrete mix. To enhance the tensile and flexural strength of hardened concrete, fibers were added, leading to the development of Fiber Reinforced Concrete (FRC)<sup>23–26</sup>. Steel fibers can contribute to significantly better crack resistance during fracture phenomenon by enhancing toughness of the structural element<sup>27–29</sup>. Using unorthodox reinforcement such as fibers can solve the issue of overcrowding at the beam column connections due to presence of hoops. Steel fiber-reinforced concrete (SFRC) presents itself as a viable alternative to traditional reinforcement. By distributing reinforcing fibers throughout the concrete matrix, SFRC can achieve comparable stability, ductility, and energy dissipation while potentially reducing reinforcement congestion and optimizing costs<sup>13</sup>. Banu et al.<sup>30</sup> conducted an experiment on beam-column joints with steel fibers to evaluate their seismic performance using reverse cyclic loading. Their findings indicate that incorporating steel fibers within the joint core can reduce reinforcement congestion. This reduction is achieved by potentially eliminating or minimizing the need for transverse reinforcement in this critical area. Additionally, the study suggests that SFRC enhances the joint's ductility and energy dissipation capacity, both of which are crucial for seismic resistance. However, their study did not investigate SFRC beam-column connections without hoops in the joint core region. Zhang et al.<sup>31</sup> explored the seismic response of precast interior beam-column connections with steel fibers. They concluded that by using steel fibers precast joints can exhibit greater shear resistance when subjected to seismic loadings. They inferred that anchorage length can be minimized by using steel fibers thereby improving bond strength accompanied with minimization of core confinement reinforcement required. The performance of precast structural members and cast-in-situ structural members can differ significantly due to factors such as poor workmanship, substandard material quality, and labor negligence. Consequently, they did not include cast-in-situ beam-column joint specimens in their studies. Patel et al.<sup>32</sup> investigated both conventional reinforced concrete and SFRC beam column connections. Their research indicated that the SFRC joints can sustain greater displacements without generating greater cracks and they found out that SFRC in joints can enhance dimensional stability. For the joints subjected to cyclic loading the stiffness degradation happened with slower rate in the connections with SFRC than the connections with simple RC. They also suggested that by using SFRC in joint lateral reinforcement can be reduced in joint core region. However, they didn't examine the effect of varying volume fraction of steel fibers on the results. Noor et al.<sup>33</sup> employed cyclic analysis to explore the seismic behavior of SFRC beam-column joints. Their research highlighted that incorporating steel fibers within the concrete matrix can enhance its mechanical properties. This improvement encompasses increased compressive, tensile, and flexural strengths, but it is contingent upon using an optimal fiber volume and maintaining a suitable water-to-cement ratio. If not, the steel fibers could negatively impact the matrix properties. They also discovered that an optimal amount of steel fibers increased the connection's load-bearing capacity, ductility, and overall load-carrying performance of the joint. However, they did not explore how variations in steel fiber aspect ratio influence the post-cracking behavior of SFRC beam-column joints.

Physical testing and experimentation of structural components and assemblies is quite time consuming and costly. Furthermore, it is prone to human errors in labs and on sites which can cause inaccuracy in results. Finite element analysis is being widely used to analyze the structural components under various loading conditions. It can minimize or reduce the cost of testing and enhance the accuracy of results. By using 3D FEM techniques time required for physical testing can also be saved in an effective and efficient way<sup>34</sup>. The 3D FEM techniques portray an added comprehensive and precise illustration of the structural configuration and reinforcement organization along with its interaction with concrete<sup>35</sup>. Shi et al.<sup>10</sup> employed 3D finite element analysis to investigate the seismic behavior of steel fiber-reinforced concrete (SFRC) beam-column joints. Their study explored the influence of various parameters, including concrete compressive strength, steel fiber content, and transverse reinforcement spacing within the joint core. The analysis indicated that while increasing concrete strength led to a marginal improvement in peak load capacity, it came at the expense of reduced ductility. Conversely, incorporating steel fibers demonstrably enhanced the joint's seismic performance. Additionally, the study suggested that widening the spacing of transverse hoops could mitigate congestion in the joint core. However, Shi et al. did not address the impact of varying steel fiber aspect ratios on both ductility and post-cracking behavior within the joint core, leaving this as a potential area for further investigation. Yimer et al.<sup>36</sup> conducted a numerical investigation on SFRC beam-column joints, simulating their behavior under seismic loading. Their findings suggest that incorporating approximately 2% steel fiber volume within the joint core can potentially eliminate the need for stirrups in this critical region, leading to improved seismic performance. The study also highlights the benefits of SFRC in enhancing the joint's stiffness, load-bearing capacity, ductility, and energy absorption capacity. Notably, Yimer et al. observed a significant reduction in shear cracks within the core area subjected to seismic activity. However, their research did not address the optimal size of steel fibers for maximizing post-cracking behavior in the beam-column connection through the crack-bridging mechanism of the fibers. Abusafaqa et al.<sup>37</sup> worked on sway special outer beam column connection. They proposed from their research that the use of steel fibers can minimize the crowding of core region of beam column connection due to the hoops required as per sway special design criteria. They also inferred that by using steel fibers strength and ductility of the joint can be enhanced for connections with high beam to column depth ratios. However, they didn't examine the effect of volume fraction on the cyclic stiffness degradation of the specimen. Abbas et al.<sup>13</sup> explored the seismic response of SFRC joints and inferred that augmenting the fiber volume fraction resulted in increased joint strength. Additionally, they observed an enhancement in the bond strength between the matrix and rebars, crucial for seismic design. They also cautioned against an excessive amount of steel fibers, as it could result in a less ductile response. However, they did not investigate the impact of varying the diameter of steel fibers in their study.

The present research evaluated the parametric analysis of steel fibers reinforced beam column joint by using finite element analysis techniques in ABAQUS software. In this study, the impact of steel fibers volume fraction (VF) and different aspect ratios ( $l/d$ ) (shown in Table 1) on the load deflection behavior of SFRC beam-column joint and crack propagation along with post cracking behavior is assessed. For this purpose, an experimental data of Baloch et al.<sup>38</sup> is used to calibrate the model. After successful calibration, the parametric analysis is carried out. The amount of steel fibers that can be used in the matrix ranges between 0.5 and 2.5% by volume of concrete<sup>39</sup>. So, the parametric analysis to figure out the optimum amount of steel fibers to be used in the matrix is carried out using different amounts of steel fibers i.e., 0.5%, 1%, 1.5%, 2%, and 2.5% by volume of concrete respectively. The steel fibers volume fraction which showed the best load deflection behavior are further used for the parametric analysis of different aspect ratios to figure out the optimum one. The length of Steel fiber ranges from 15 to 75 mm (1/4 to 3 inches) and aspect ratio ( $l/d$ ) ranges from 30 to 100<sup>39</sup>. For parametric analysis of Aspect Ratio, five different ( $l/d$ ) ratios of 35, 50, 64.23, 75 and 91.67 are used.

## Experimental test

Balouch et al.<sup>38</sup> conducted an experiment to evaluate the response of steel fiber reinforced concrete beam-column connections under cyclic loading. This study focused exclusively on the performance of hooked-end steel fibers, as depicted in Fig. 6. The prototype used in the experiment was scaled down to half-size. To obtain reasonable rebar sizes, the steel areas were rounded to approximately half of those in the full-scale joint. The cross-sections of the beam and column used in the experiment are shown in Fig. 1. The distribution of steel fibers and plain concrete is illustrated in Fig. 2. Also, the terminologies used for depth and width for the beam and Column are  $h_b$  is overall depth of beam,  $b_c$  is width of column and  $h_c$  is overall depth of column.

For loading, a displacement-controlled quasi-static hysteric method was selected, as recommended by FEMA-461 (Federal Emergency Management Agency), as it provides a more accurate representation of seismic loads. FEMA-461 establishes interim protocols for assessing the seismic performance characteristics of structural and nonstructural components<sup>40</sup>. The cyclic displacement loading scheme involved incrementally doubling the

Aspect Ratio	Length (mm)	Diameter (mm)
35	35	1
50	45	0.9
75	60	0.8
85.71	60	0.7
91.67	55	0.6

**Table 1.** Aspect Ratio used for Parametric Analysis.

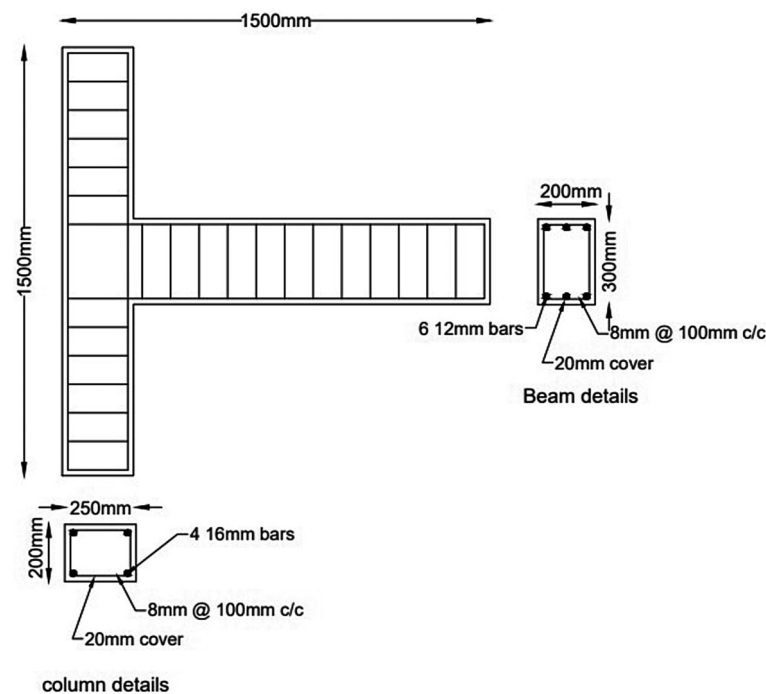


**Figure 1.** Beam Column Joint details.

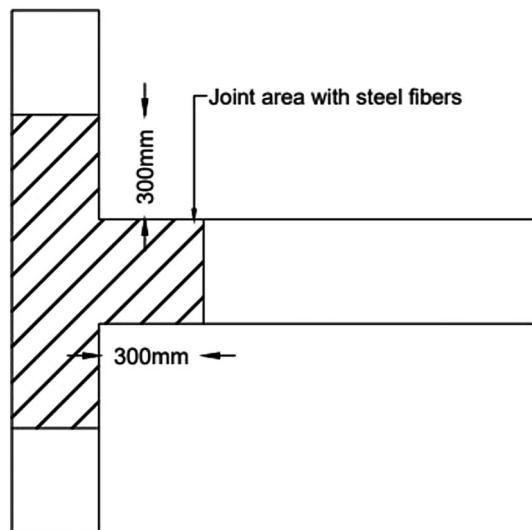


**Figure 2.** SFRC Joint–Central portion with hooked steel fibers.

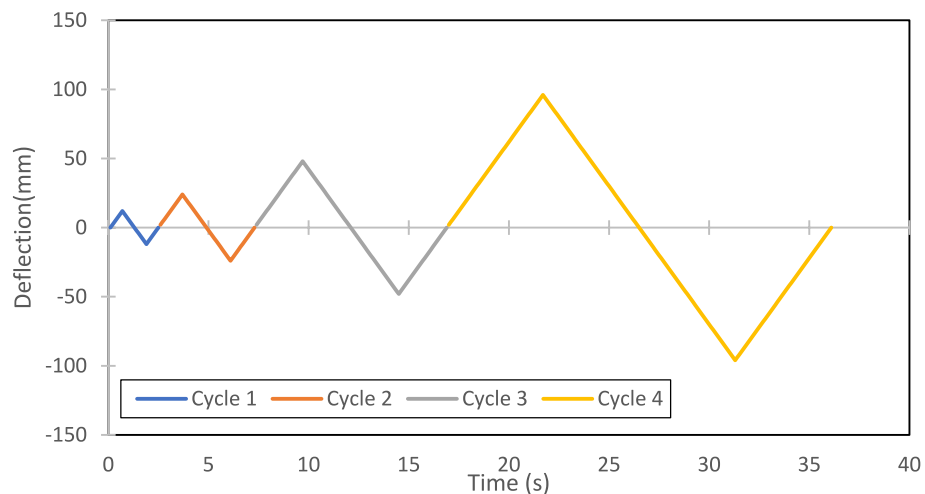


**Figure 3.** Cyclic loading pattern.

displacement with each cycle, starting with 12 mm and progressing to 24 mm, 48 mm, and finally 96 mm. As depicted in Fig. 3, the loading was applied over four cycles.

Figure 4 illustrates the experimental setup, where gauges attached to the hydraulic jacks and computer terminals monitored the loading and displacement throughout the testing process. This data was subsequently converted into Excel files for further analysis, plotting, and ultimately used in the present study for validating the finite element (FE) model against real-time experimental results. As a consequence of the loading, the joint experienced permanent deformation, also known as residual displacement, arising from the formation of residual or plastic strains (circled in Fig. 5). For reference, the material properties employed in this study are tabulated in Table 2.

Beam column connections govern the integrity of the structural systems under seismic activity. Strong column and weak beam design philosophy is adopted to make the beam yield before the connection to ensure a joint failure of ductile shear nature rather than a joint failure of brittle nature. It is the one in which the beam does not yield first, and connection undergoes plastic deformation first due to formation of residual strains and loses its elasticity resulting in abrupt failure of the whole structure<sup>41</sup>.

Lack of hoops in the joint core area, use of undeformed rebars, loss of bond strength between concrete and steel, lack of ductility in the joint and poor anchorage details are the main reasons to cause a brittle or non-ductile shear failure of the joint<sup>42</sup>. The Shear damage in the joint is exhibited by formation of shear hinges in joint core region (Fig. 6). The reduced stiffness of the beam column joint due to formation of shear hinges can trigger the soft story mechanism ultimately resulting in collapse of the structure<sup>43</sup>. The failure mechanism of joint (Concrete wedge mechanism) can be observed in Fig. 7.



**Figure 4.** Beam column joint Before loading.

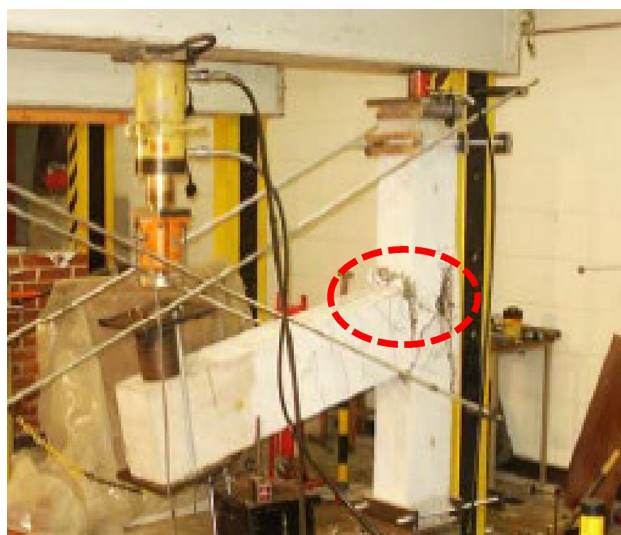


**Figure 5.** Beam Column Joint after loading.

Steel fibers properties (hooked end)	
Length (mm)	35
Aspect ratio	65
Diameter (mm)	0.55
Tensile strength (N/mm <sup>2</sup> )	1300
SFRC properties	
Tensile strength (Mpa)	3.6
Compressive strength (Mpa)	3.6
Rebars properties	
Yield strength (N/mm <sup>2</sup> )	50
Plain concrete Properties	
Tensile strength (Mpa)	3.7
Compressive strength (Mpa)	45

**Table 2.** Properties used in control specimen.

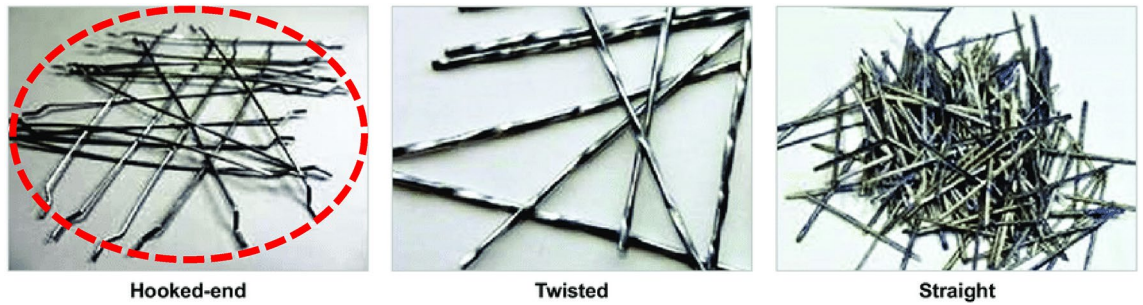


Figure 6. Steel fibers type used in experiment.

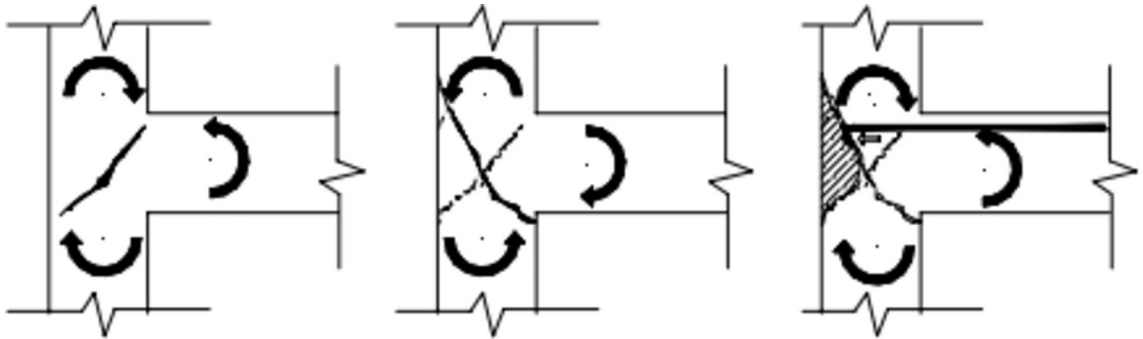


Figure 7. Concrete wedge mechanism.

By using SFRC the strength of beam column connection can be enhanced under seismic activity as the ductility and energy dissipation (due to crack bridging mechanism) of the connection can be significantly improved to ensure a ductile shear failure<sup>44</sup>. Due to higher amount of elastic recovery energy SFRC beam column connections can perform better in seismic activity and have a greater strength. By using SFRC, elimination or reduction of the transverse reinforcement can ease the congestion issues of the joint<sup>45</sup>. Bond strength and anchorage of steel bars can be enhanced by 30% by using SFRC<sup>46</sup>.

### Validation of FE model with experiment

#### Development of FE model

The assembly of 3d NLFEA model was prepared according to the experimental prototype<sup>38</sup>. The geometries of different segments of the numerical model were created in part module of the ABAQUS (student learning edition, <https://www.3ds.com/edu/education/students/solutions/abaqus-le>) tool by using several built-in commands. The dimensions of each part are given in Table 3. The created parts were arranged according to experimental setup<sup>38</sup>, by using assembly module and different partitions, data points, interacting surfaces and sets of same type of elements were also generated. The geometry of the model created in ABAQUS is shown in Figs. 13 and 14.

Engineered stress strain curves created by using different constitutive models were implied to predict the mechanical response of materials that are to be used in 3d NLFEA model. Stress strain response of three materials i.e., plain concrete (PC), steel fibers reinforced concrete (SFRC) and steel (reinforcement and steel plates) was modelled by using different constitutive models which is described below:

The elastic response of concrete was modeled using the modulus of elasticity and Poisson's ratio of concrete. The plastic behavior was modeled using the constitutive laws proposed in the Eurocode for plain concrete under

Part	Length (mm)	Width (mm)	Depth (mm)	Diameter (mm)	Nos	Spacing
Beam	1250	200	300	N/A	N/A	N/A
Column	1500	200	250	N/A	N/A	N/A
Column rebars	1460	N/A	N/A	16	4	N/A
Beam rebars	1460	N/A	N/A	12	6	N/A
Steel plates	250	200	50	N/A	N/A	N/A
Stirrups	N/A	160	260	8	N/A	100 mm @ c/c
Ties	N/A	160	210	8	N/A	100 mm @ c/c

Table 3. Dimensions of control model.

compression and tension, generating an engineered stress–strain curve. Following constitutive law from the Euro code was implied to model the plastic compressive response of plain concrete:

$$\sigma = f_{cm} * \frac{k\eta - \eta^2}{1 + (k - 2)\eta},$$

$$k = 1.05 * E_{cm} * \frac{\epsilon_0}{f_{cm}},$$

$$\eta = \frac{\epsilon}{\epsilon_0},$$

$$\epsilon_0 = 0.7f_{cm}^{0.31}.$$

where  $\sigma$  is compressive stress at a point,  $f_{cm}$  is peak compressive strength of the concrete,  $\epsilon_0$  is strain against peak strength of the concrete,  $\epsilon$  is strain at a point,  $k$  is a function of peak elastic behavior of concrete and  $\eta$  is ratio of strain at a point to peak strain of concrete and  $E_{cm}$  is the elastic modulus of concrete.

Similarly, the constitutive law used to capture the plastic tensile response of concrete is as under:

$$f_{t0} = 0.3 * f_{cm}^{\left(\frac{2}{3}\right)},$$

$$f_t = f_t \left( \frac{\epsilon_{cr}}{\epsilon_t} \right)^{0.4}.$$

where  $f_{t0}$  is tensile strength of concrete,  $f_t$  is tensile stress at a point,  $\epsilon_{cr}$  is strain at tensile strength and  $\epsilon_t$  is strain at a point. All the variables used in above mentioned constitutive laws were used according to the experimental

Variable used	Value used
$f_{cm}$	45 Mpa
$\epsilon_0$	0.002
$E_{cm}$	31,528.55 Mpa
$f_{t0}$	3.79 Mpa
$\epsilon_{cr}$	0.0001
Density	2.54e-009 ton/mm <sup>3</sup>
Poisson's ratio	0.22

**Table 4.** Variables used in modelling of conventional concrete.

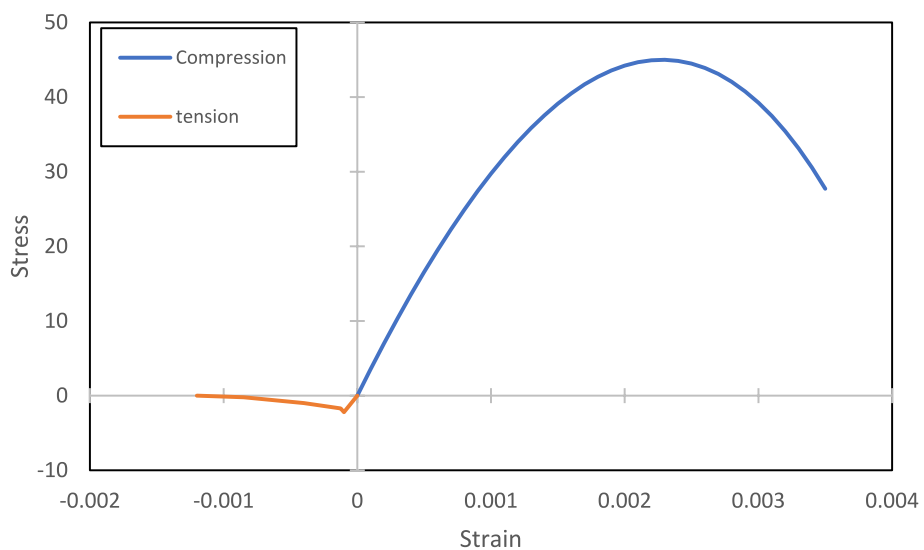


**Figure 8.** Stress–Strain Behavior of Plain Concrete in Compression and Tension.

data of Balouch et al.<sup>38</sup>. Table 4 represents the variables used in modelling of conventional concrete. Engineered stress strain curve used to define PC is shown in Fig. 8.

### Steel fibers reinforced concrete

Constitutive models presented by Ezeldin et al.<sup>46</sup> and Moradi et al.<sup>47</sup> were used to model the plastic compressive and tensile behavior of SFRC respectively and to produce engineered stress strain curve whereas the elastic behavior was modelled using the Poisson's ratio and modulus of elasticity. Constitutive law used to model the compressive behavior of SFRC is as under<sup>46</sup>:

$$\frac{\sigma_c}{f_c'} = \beta * \frac{\left(\frac{\varepsilon_c}{\varepsilon_{c0}}\right)}{\beta - 1 + \left(\frac{\varepsilon_c}{\varepsilon_{c0}}\right)^\beta},$$

$$\beta = 1.093 + 0.7132(RI)^{-0.926},$$

$$RI = wf * \frac{l_f}{d_f},$$

$$wf = 3 * v_f,$$

$$\varepsilon_{c0} = \varepsilon_0 + 446 * 10^{-6} * (RI).$$

where  $\sigma_c$  is stress at a point,  $f_c'$  is compressive strength of SFRC,  $\beta$  is the influence of fibers on the matrix,  $\varepsilon_c$  is strain at a point,  $\varepsilon_{c0}$  is strain against compressive strength of SFRC, RI is reinforcing index of steel fibers,  $w_f$ ,  $l_f$ ,  $d_f$  and  $v_f$  is weight of fibers, length of fibers, diameter of fibers and volume of fibers respectively and  $\varepsilon_0$  is peak strain of plain concrete.

Similarly, Moradi et al.<sup>47</sup> proposed a constitutive law for modelling plastic tensile behavior of SFRC which is as follows:

$$\sigma_t = f_{tf} * \left( \frac{\left(\frac{\varepsilon}{\varepsilon_{fmax}}\right)}{\left(0.33 * \left(\frac{\varepsilon}{\varepsilon_{fmax}}\right)^{0.33}\right) + 0.67} \right) \text{ when } (\varepsilon < \varepsilon_{fmax}),$$

$$\sigma_t = f_{tf} * \left( \frac{\left(\frac{\varepsilon}{\varepsilon_{fmax}}\right)}{\left(\alpha * \left(\frac{\varepsilon}{\varepsilon_{fmax}} - 1\right)^{1.7}\right) + \left(\frac{\varepsilon}{\varepsilon_{fmax}}\right)} \right) \text{ when } (\varepsilon > \varepsilon_{fmax}),$$

$$\alpha = 0.22f_c'0.56 \left( 1 + \left( \frac{v_f}{100} * \frac{l_f}{d_f} \right) \right)^{-1.74}$$

$$f_{tf} = 0.54 * (f_c')^{\frac{1}{2}},$$

$$\varepsilon = \frac{f_{tf}}{E},$$

$$E = \left( 3300 * f_c'^{\frac{1}{2}} + 6900 \right) * \left( \frac{\gamma_c}{23} \right)^{1.5}.$$

where  $\sigma_t$  is tensile stress at a point,  $f_{tf}$  is tensile strength of SFRC,  $\varepsilon$  is strain at a point,  $\varepsilon_{fmax}$  is strain against tensile strength,  $\alpha$  is influence of steel fibers,  $f_c'$  is compressive strength of fibrous concrete and  $\gamma_c$  is density of fibrous concrete.

The variables used in modelling the behavior of SFRC in above mentioned constitutive laws were according to the experimental data of Balouch et al.<sup>38</sup>. Table 5 represents the variables used in modelling of SFRC whereas engineered stress strain curve of SFRC is shown in Fig. 9.

### Steel

According to Fayed et al.<sup>1</sup> the mechanical behavior of steel rebars and steel plate can be modelled using an elastic perfectly plastic approach directly in ABAQUS. Kinematic hardening as well as isotropic hardening can be used while defining steel material. As the elastic perfectly plastic model is being used to model steel, it does not consider the hardening branch of the stress strain curve of steel. This study employed material properties like steel's density, Poisson's ratio, and modulus of elasticity to define the elastic region of the stress-strain behavior

Parameters used	Value used
$f_{cr}$	46 Mpa
$l_f$	35 mm
$d_f$	0.55 mm
$V_f$	0.92%
$\epsilon_0$	0.002
$f_{ff}$	3.66 MPA
$\epsilon_{fmax}$	0.00012
Density	2.4e-009 ton/mm <sup>3</sup>
Poisson's ratio	0.2
$E_{cm}$	31,876.95 Mpa

**Table 5.** Variables used in modelling of SFRC.

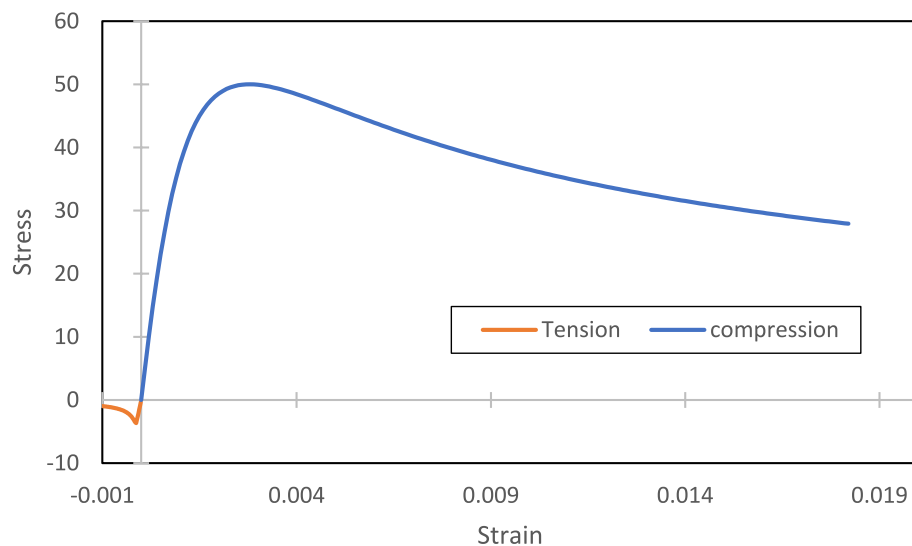


**Figure 9.** Stress–strain behavior of SFRC in compression and tension.

for steel rebars. Conversely, the plastic region was characterized using the yield strength and plastic strain at yield of the rebars. Mechanical behavior of steel plates was also modelled in the same way but the plastic behavior was not defined because the steel plates were mainly used in FEA model to demonstrate the experimental setup in which steel plates were used as fixed supports and as loading plates in order to avoid direct loading on the sample for the sake of accuracy of experiment and to keep the prototype fixed in one position during the loading so the deformation of steel plates is not required and wanted. The parameters used in elastic perfectly plastic bilinear model to demonstrate mechanical behavior of steel are given in Table 6.

### Material property

The Concrete Damaged Plasticity (CDP) (32) model, as documented in the ABAQUS user manuals, was adopted to represent the quasi-brittle behavior of reinforced concrete (RC) and steel fiber-reinforced concrete (SFRC) in this study. The damage parameters  $d_c$  and  $d_t$  were calculated as per expressions below<sup>48</sup>.

Parameters used	Value used
Elastic modulus	200,000
Density	8e-009 ton/mm <sup>3</sup>
Poisson's ratio	0.3
Yield strength	500 N/mm <sup>2</sup>

**Table 6.** Parameters used in elastic perfectly plastic model.

$$d_c = 1 - \frac{f_c}{f'_c}$$

$$d_t = 1 - \frac{\sigma_t}{f_t}$$

The yielding of material is exhibited in ABAQUS via yielding function which have several important input variables. The values of these parameters used are chosen after studying extensive literature including that of<sup>16</sup> with slightest modifications to improve the accuracy of this FEA study. Among the above-mentioned parameters viscosity parameter is the most important as the convergence problems can be effectively solved while analysis thereby fluctuating viscosity parameter<sup>49</sup>. Moreover, Fig. 10 represents CDP model under tension, Fig. 11 represents CDP Model under compression and Fig. 12 represents the yield surface. The parameters used in this study are presented in the Table 7:

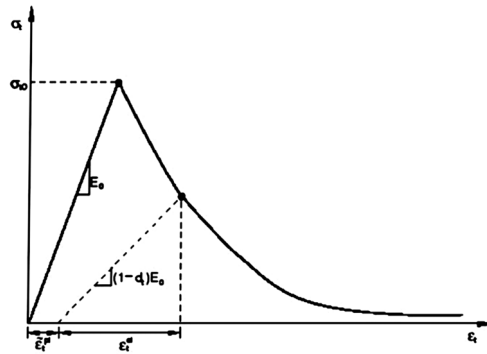


Figure 10. CDP model under tension.

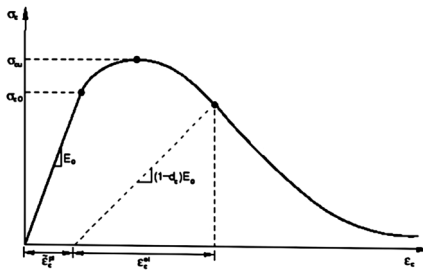


Figure 11. CDP model under compression.

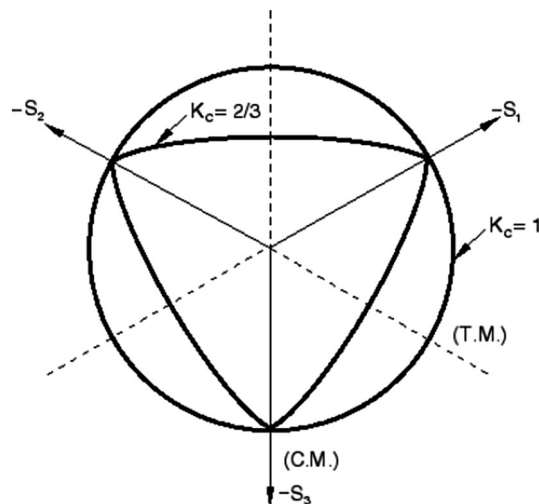
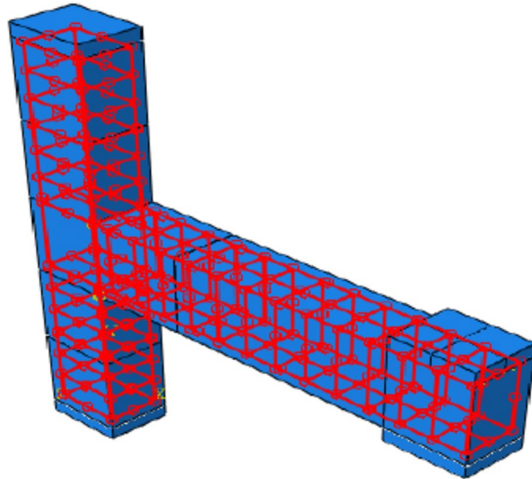


Figure 12. Yield surface.

Parameter used	Value used
Dilation angle	35
$\sigma_b/\sigma_c$	1.16
K	0.66
Eccentricity	0.1
Viscosity parameter	0.002

**Table 7.** Yield function parameters.



**Figure 13.** constraints used for rebars (embedded region).

### Interactions and loading protocol

Different parts of the model were connected to each other using different built-in constraints in constraints module of ABAQUS. Following constraints are used in this study:

- I. Tie constraint: The connection between steel plates, loading plates and BC joint is modelled by using a built-in tie constraint in ABAQUS which exhibits the real experimental setup and the connection between concrete and steel fibers reinforced concrete is also modelled as tie. Beam to column connection is also modelled as a tie constraint as it is easy to use and is widely used to connect surfaces permanently with each other<sup>50</sup>.
- II. Embedded region: Embedded region built-in constraint is used to model the steel rebars in the concrete matrix which exhibits the perfect bonding between concrete and steel. The bond slip behavior is not included in scope of this study so perfect bonding can be considered<sup>16</sup>.

From the experimental setup it can be extracted that the top and bottom of column is fixed that was modelled in ABAQUS as encastre support from the boundary conditions module of the FEA solver which acted as a fixed support and allowed zero degrees of freedom in both rotation and translation. The experimental setup employed displacement-controlled quasi-static cyclic loading (Figs. 13 and 14). The displacement-controlled quasi-static cyclic loading was modeled in ABAQUS within the boundary conditions module by selecting translation in the y-direction, represented as direction (2) in ABAQUS. The cyclic load history was defined as a ramp in tabular data form, specifying amplitude against time according to the actual loading used in the experimental setup. Five loading cycles with increasing amplitudes were used to run the model to capture the hysteretic capacity curve, calibrating the FEA model with the actual hysteretic response of the beam-column joint. Figure 15 illustrates the boundary conditions and loading applied to the model.

### Element types

To mesh the FEA model into several elements and nodes two different types of elements were selected for concrete, SFRC, steel plates and rebars in the FEA study. For solid family of members including PC, SFRC and steel plates C3D8R that is brick-like (Collapsed 3d 8 noded reduced integrated) element type was used while for truss family of members that is rebars, stirrups and ties a T3D2 (Truss 3d 2 noded) that is line-like element type was used (3). The mesh size was used as 50 mm for the sake of accuracy. The accuracy of the analysis is greatly dependent on the element types and mesh size. More complex element types such as tetrahedral with more nodes can add to the accuracy of the analysis but it will take a significantly greater amount of time to run the analysis and mesh size is also directly related to accuracy and time of the analysis. The hourglass effect (zero

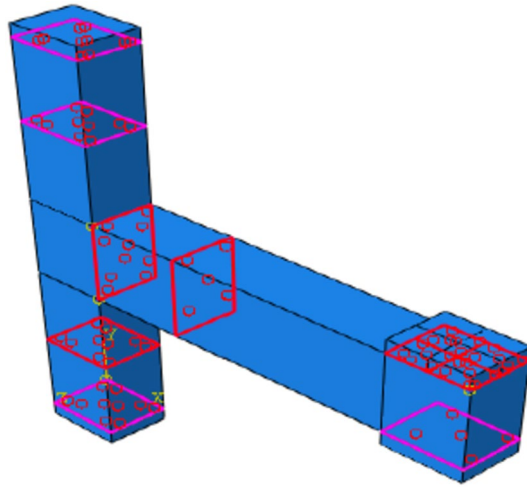


**Figure 14.** constraints used for Junctions (Tie Connection).

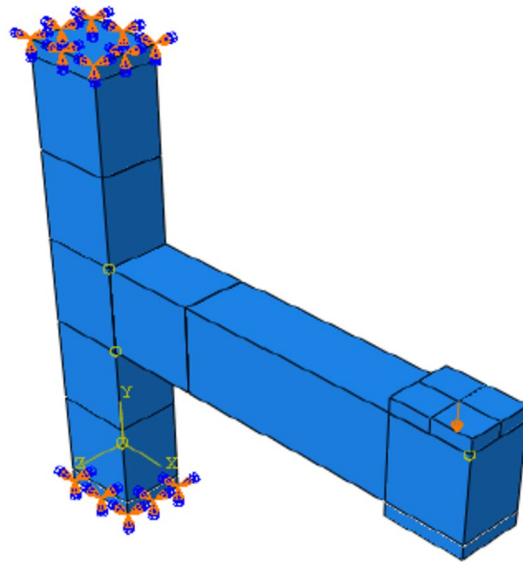


**Figure 15.** Boundary Conditions and loading.

energy mode) option was set to default during this FEA study. The hourglass effect can be considered depending upon the type of material used in the analysis. Figure 16 represents meshing of steel fiber reinforced concrete and plain concrete while Fig. 17 represents meshing of rebars.

## Results

### Investigation on viscosity parameter

The viscosity parameter is investigated for the sake of accuracy of the model (37). Different viscosity parameters were used, and the result (hysteric loop) was accumulated for only 1st cycle to pick up the parameter which is closely in match with the experimental study.

An analogy of the FEA and the experimental findings related to the load–deflection response is shown in Fig. 18. During the analysis, the viscosity parameter was carefully adjusted to ensure accurate and stable results. Initially, a range of values from 0 to 0.01 was tested, including 0.001, 0.002, and 0.004. For the default value of 0, the analysis failed to converge and ended prematurely, highlighting the necessity of incorporating a non-zero viscosity parameter.

Given the high nonlinearities in the modeling, the time increment step was set to automatic to handle the complexities effectively. Through iterative testing, it was observed that smaller values of the viscosity parameter, specifically 0.002 and 0.004, provided results that closely matched the experimental data in terms of hysteric ultimate load and deflection.

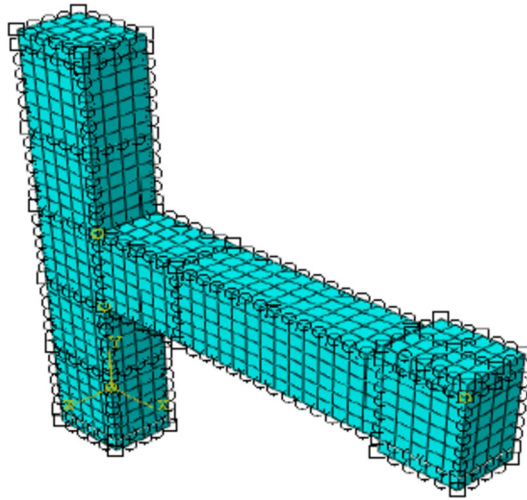


**Figure 16.** Meshing of SFRC and PC.

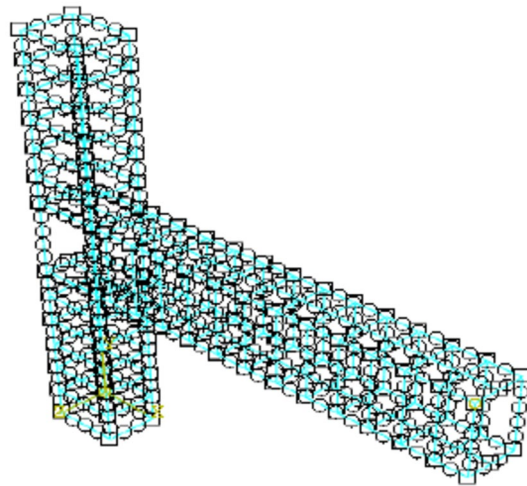


**Figure 17.** Meshing of rebars.

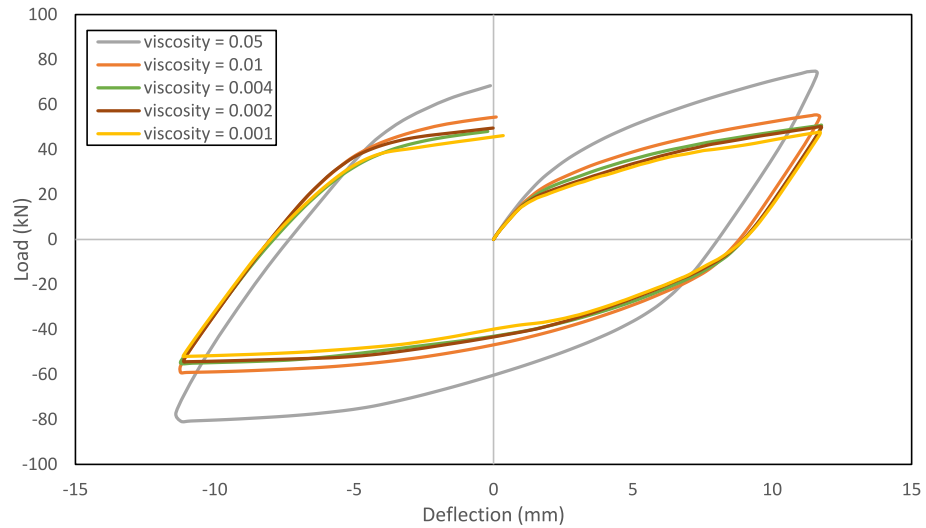
The primary goal was to improve the rate of convergence without significantly compromising the model's accuracy. The introduction of small viscosity values facilitated larger stable time increments, which accelerated the computation process. However, increasing the viscosity parameter to 0.01 resulted in overestimation of the specimen's stiffness and strength, indicating a trade-off between computational efficiency and model accuracy.

Figure 18 illustrates that an excessively high viscosity parameter can lead to inaccurate predictions. Consequently, the viscosity parameter must be selected with extreme care when using the CDP model in calculations. The findings suggest that a properly calibrated viscosity parameter not only shortens analysis times but also enhances the model's predictive capabilities, aligning with the understanding that internal friction is a key factor in the plastic deformation of concrete elements.

Based on these observations, a viscosity parameter of 0.002 was chosen for all subsequent analyses. This value was selected after it was found to replicate the load observed in the experiment's first cycle, which was 50.16. As shown in Table 8, using a viscosity parameter of 0.002 resulted in a load of 50.16 in the first cycle, thereby validating its appropriateness for the model.

### FE result verification

The beam-column joint subjected to cyclic loading was selected as an experimental prototype to conduct the verification study, focusing on the load–deflection response and the failure patterns observed in both the real experiment and the FEA model.



**Figure 18.** Effect of different viscosity parameter.

Viscosity parameter	Cycle	Peak load (kN)
Exp Test	1st	50.16
0.05	1st	74.63
0.01	1st	55.40
0.004	1st	50.72
0.002	1st	50.16
0.001	1st	46.95

**Table 8.** Peak load of different Viscosity parameters in the 1st cycle.

### Peak load–deflection response

Figures 19 and 20 compare the hysteretic and skeletal curves from FEA with the outcomes of the experiments, respectively. The peak load–deflection results from FEA are well-aligned with those from the experiments. In real time experimentation there are minute little micro cracks present in the material at microscopic level which are not taken into consideration while performing FEA<sup>51</sup>. In comparison with the experimental results, the FEA model accurately depicted the skeleton curve. The bond slip law between concrete and steel was not

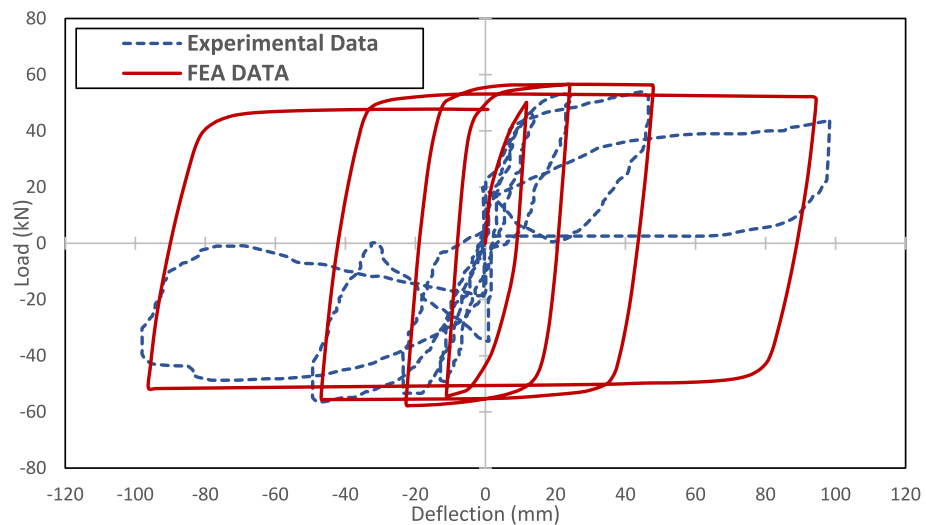


**Figure 19.** Hysteresis curve of calibrated model.

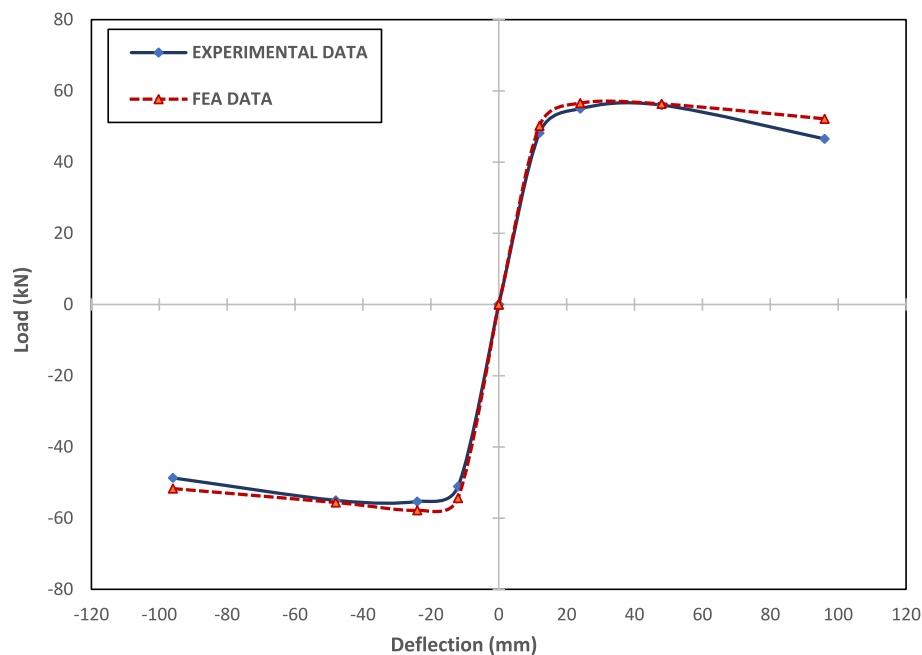


**Figure 20.** Skeleton curve of experimental vs FEA data.

implied in the present study rather an embedded region constraint was implied to define the bond relation. Due to the mentioned limitations in the present study a fat pinching response was captured in the hysteretic load vs deflection curves. This difference between the FEA and experimental results is due to the method of embedded region used to define the interaction between concrete and steel as the focus in this study is joint ductility and not the bond slip between concrete and steel and it can be minimized by defining a bond slip constitutive model. To quantify the model's overall accuracy and average error, the percentage error and mean model accuracy (M (%)) were calculated using the following expressions.

$$\text{Error}(\%) = \left[ \frac{\text{FEAresult} - \text{TestResult}}{\text{Testresult}} \right] \times 100$$

$$\text{Mean Model Accuracy} (\%) = \left[ \frac{\text{FEAresult}}{\text{Testresult}} \right] \times 100$$

The maximum load obtained from the FEA of specimen SFRC-VF-0.92 (Calibrated Model) is 8.62% higher than that of the experimental study, as shown in Table 9.

Table 9 represents an 8% average error in the FEA in accordance with real experimentation performed that indicated a decent agreement of FEA with real experimental study. The behavior of the model obtained through FEA simulations was quietly matching with the results obtained through the experimentation.

In general, both curves showed a respectable level of agreement. The FE curve showed behavior that was somewhat higher than the experimental curve for all cycles. This higher behavior is due to the impact of the assumed variables, absence of bond slip law and on-site real conditions of the material absent in FEA modelling phase.

The finite element (FE) model of the SFRC beam-column connection successfully predicted the load–deflection behavior of the connection under cyclic loading with high accuracy. Table 10 shows the comparison of experimental data and data driven from ABAQUS.

Overall, the FEA results in each cycle are quite like experimental results. The maximum error is in the 4th cycle, which is 10%, which is acceptable for such kind of models<sup>52</sup>.

Specimen	Average maximum load (kN)		Prediction	
	FEA	Experimental test	error (%)	M (%)
SFRC-VF-0.92	53.80	49.53	8.62	108.62

**Table 9.** Maximum load comparisons of FEA with the experimental results.

	FEA data	Experimental data		Error (%) in each cycle	
	$\Delta$ (mm)	P (kN)	$\Delta$ (mm)		P (kN)
<i>Positive cycles</i>					
1ST cycle	12	48.15	12	50.16	4.01
2ND cycle	24	55	24	56.55	2.75
3RD cycle	48	56	48	56.34	0.60
4TH cycle	96	46.8	96	52.14	10.24
<i>Negative cycles</i>					
1ST cycle	-12	-51.12	-12	-54.38	6.00
2ND cycle	-24	-55.34	-24	-57.81	4.28
3RD cycle	-48	-55.01	-48	-55.61	1.09
4TH cycle	-96	-48.71	-96	-51.70	5.79

**Table 10.** Error (%) in each cycle.

The behavior of the specimen obtained through FEA demonstrated that the chosen material parameters and constitutive laws could accurately estimate the behavior of the beam-column connection. However, due to the complexities involved in numerical modeling, it is essential to examine the impact of the selected model parameters on the accuracy of the analysis.

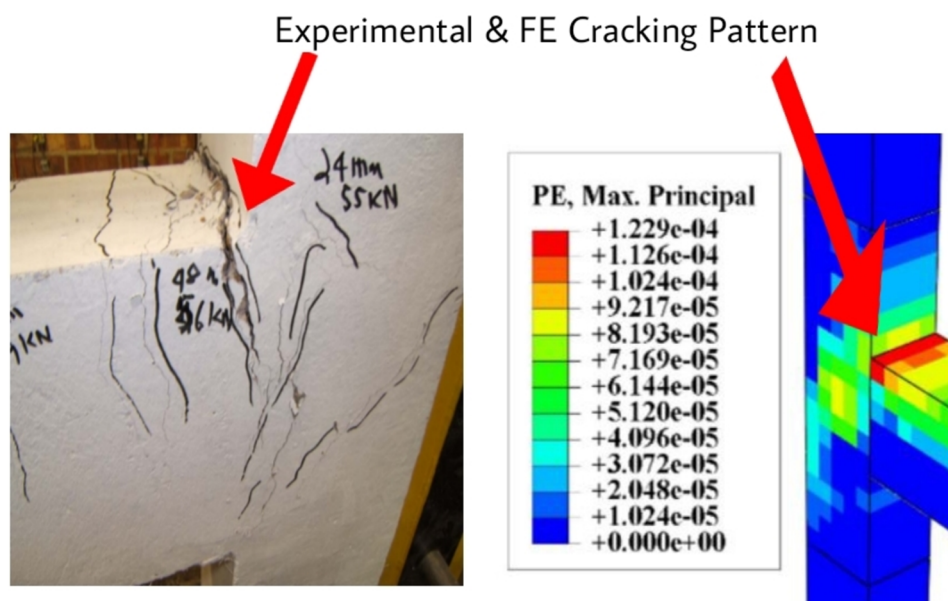
### Crack pattern

Figure 21 compares the initial crack patterns predicted by the finite element (FE) model with those observed in the experiment. The FE model exhibited a high degree of accuracy in capturing the crack distribution. Cracks appeared at the same locations and followed similar propagation patterns as seen in the experimental results. This successful prediction can likely be attributed to the adoption of a strong column-weak beam design approach in the experiment. Overall, these findings validate the FE model's capability to reliably simulate the experimentally observed failure patterns.

### Details of models for parametric study

In this research article, the beam-column joint specimen tested is based on the study conducted by Balouch et al., which serves as the foundation for the present study. The SFRC-VF-0.92 specimen is selected as the control specimen and is numerically modeled and validated using experimental data. Additional specimens are created based on the control specimen to investigate the effect of varying the steel fiber volume fraction and aspect ratio in the joint panel zone.

Five different volume fractions of steel fibers (VF) are considered: 0.1%, 0.5%, 1.5%, 2%, and 2.5%. Additionally, five alternative aspect ratios of steel fibers—35, 50, 75, 85, and 91—are investigated. For the FEA of all



**Figure 21.** Failure patterns.

prototypes, the reinforcement configurations and dimensions of the beams and columns used in the experimental specimens SFRC-VF-0.92 are maintained.

The specimens and their relevant modeling parameters are fully described in Table 11. The naming convention for the specimens is based on the steel fiber composition and the used aspect ratios. The first element, "SFRC," stands for steel fiber-reinforced concrete in the joint zone. The second component, "VF," denotes the volume fraction, and "AR" denotes the aspect ratio. The subsequent digits indicate the specific fiber percentage and aspect ratio.>

## Results and discussions of the parametric study

### General behavior and failure patterns of different volume fractions

The behavior and failure patterns of concrete specimens with varying volume fractions of steel fibers were examined in this study. According to the CDP model<sup>36</sup>, the development of compressive damage can be indicative of the specimen's fracture distribution. In particular, the maximum principal plastic strain serves as a primary indicator of crack initiation and propagation<sup>52</sup>.

Figures 22, 23, 24, 25 illustrate the fracture distribution and failure patterns observed during simulations at different volume fractions. These figures are accompanied by Table 12, which presents peak load values for each specimen under both positive and negative loading cycles. Additionally, Fig. 26a provides an overview of combined hysteresis loops for all specimens, while Fig. 26b facilitates a comparative analysis of skeleton curves across the specimens.

**SFRC-VF-0.92.** The Flexural cracks initiated at the junction of SFRC and plain concrete at a displacement of 12 mm, with a peak load of 50.17 kN. As displacement increased, cracks propagated, leading to a substantial loss in load-carrying capacity and eventual failure due to beam-joint and beam failure (Figs. 22a, 23a, 24a and 25a).

**SFRC-VF-0.1.** Similar crack behavior to SFRC-VF-0.92, albeit with slightly lower load capacities. Flexural cracks initiated at the junction point at 12 mm displacement, with a peak load of 46.79 kN, indicating 7.5% lower load capacity compared to SFRC-VF-0.92. The specimen failed due to similar mechanisms observed in SFRC-VF-0.92 (Figs. 22b, 23b, 24b and 25b).

**SFRC-VF-0.5.** Crack behavior resembled SFRC-VF-0.92, albeit with marginal variations in load capacity. Flexural cracks initiated at the junction point at 12 mm displacement, with a peak load of 48.8 kN (3% lower than SFRC-VF-0.92). Failure mechanisms were consistent with SFRC-VF-0.92 (Figs. 22c, 23c, 24c and 25c).

**SFRC-VF-1.5.** Crack behavior closely mirrored that of SFRC-VF-0.92. Flexural cracks initiated similarly at 12 mm displacement, with a peak load of 51.39 kN (2.5% higher than SFRC-VF-0.92). Specimen failure occurred via mechanisms akin to SFRC-VF-0.92 (Figs. 22d, 23d, 24d and 25d).

**SFRC-VF-2.** Crack behavior resembled SFRC-VF-0.92, with higher load-carrying capacity. Flexural cracks initiated similarly at 12 mm displacement, with a peak load of 51.78 kN (3.5% higher than SFRC-VF-0.92). Failure mechanisms were consistent with SFRC-VF-0.92 (Figs. 22e, 23e, 24e, and 25e).

**SFRC-VF-2.5.** Crack behavior identical to SFRC-VF-2, indicating similar performance. Flexural cracks initiated similarly at 12 mm displacement, with a peak load of 51.87 kN (3.5% higher than SFRC-VF-0.92). Failure mechanisms were consistent with SFRC-VF-0.92 (Figs. 22f, 23f, 24f and 25f).

Specimen	Beam			Column			VF (%)	Aspect ratio
	Cross section (mm)	Bars top and bottom (mm)	stirrups (mm)	Cross section (mm)	Bars (mm)	Stirrups (mm)		
	bb × hb			bc × hc				
SFRC-VF-0.92(Control)	200 × 300	6 × 12 mm	8 mm	250 × 200	4 × 16 mm	8 mm	0.92	64
SFRC-VF-0.1	200 × 300	6 × 12 mm	8 mm	250 × 200	4 × 16 mm	8 mm	0.1	64
SFRC-VF-0.5	200 × 300	6 × 12 mm	8 mm	250 × 200	4 × 16 mm	8 mm	0.5	64
SFRC-VF-1.5	200 × 300	6 × 12 mm	8 mm	250 × 200	4 × 16 mm	8 mm	1.5	64
SFRC-VF-2	200 × 300	6 × 12 mm	8 mm	250 × 200	4 × 16 mm	8 mm	2	64
SFRC-VF-2.5	200 × 300	6 × 12 mm	8 mm	250 × 200	4 × 16 mm	8 mm	2.5	64
SFRC-AR-35	200 × 300	6 × 12 mm	8 mm	250 × 200	4 × 16 mm	8 mm	2	35
SFRC-AR-50	200 × 300	6 × 12 mm	8 mm	250 × 200	4 × 16 mm	8 mm	2	50
SFRC-AR-75	200 × 300	6 × 12 mm	8 mm	250 × 200	4 × 16 mm	8 mm	2	75
SFRC-AR-85	200 × 300	6 × 12 mm	8 mm	250 × 200	4 × 16 mm	8 mm	2	85.7
SFRC-AR-91	200 × 300	6 × 12 mm	8 mm	250 × 200	4 × 16 mm	8 mm	2	91.6

**Table 11.** Variables and details of all specimens considered in the parametric study.

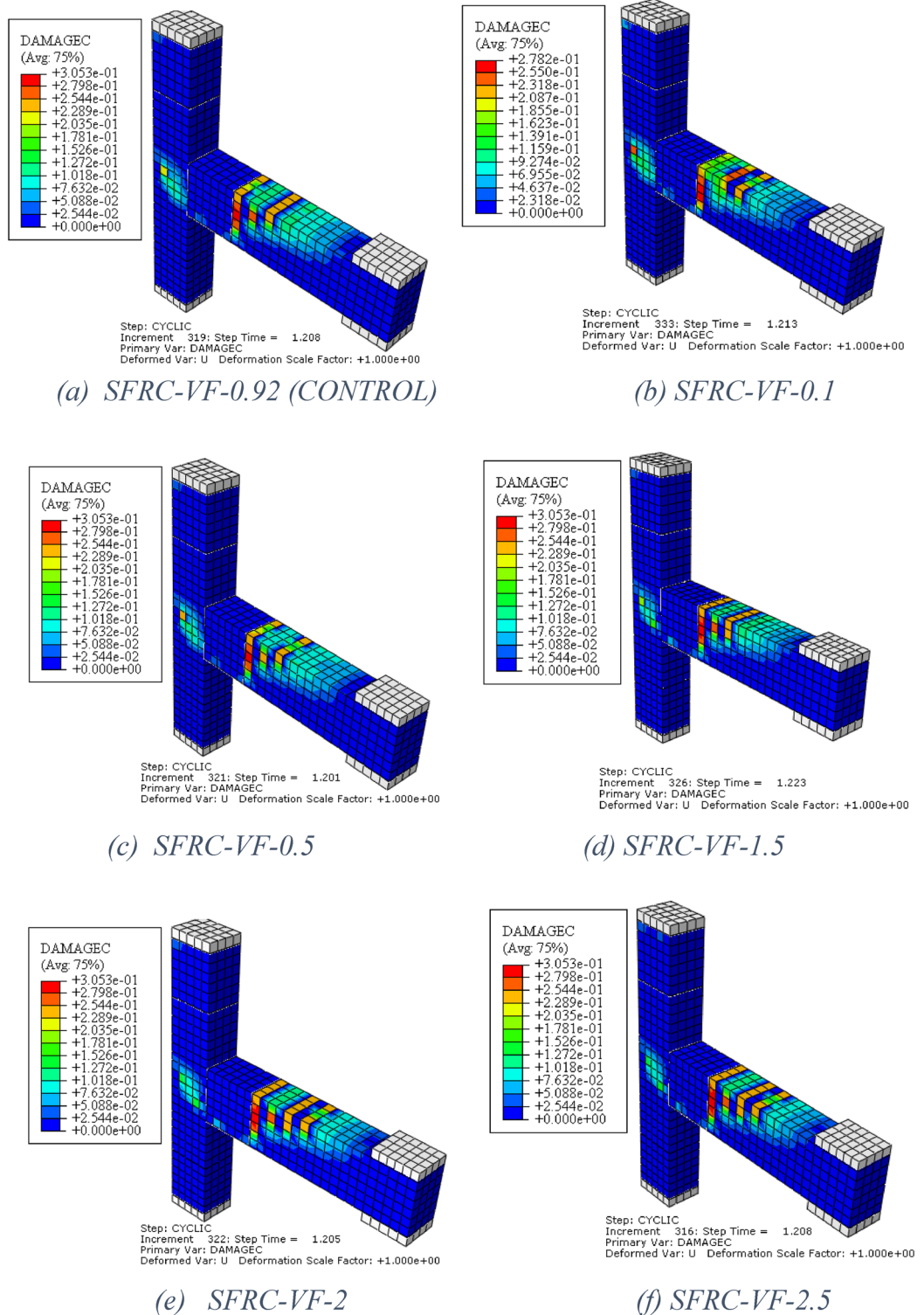


**Figure 22.** Crack patterns of the simulated specimens of VF corresponding to 1st cycle(12 mm).

This analysis underscores the impact of varying volume fractions of steel fibers on crack formation and load-carrying capacity. Notably, specimens with lower volume fractions experienced faster crack propagation and reduced load capacities, while higher volume fractions provided enhanced crack resistance and load-carrying capacity, aligning with findings from previous studies<sup>33</sup>.

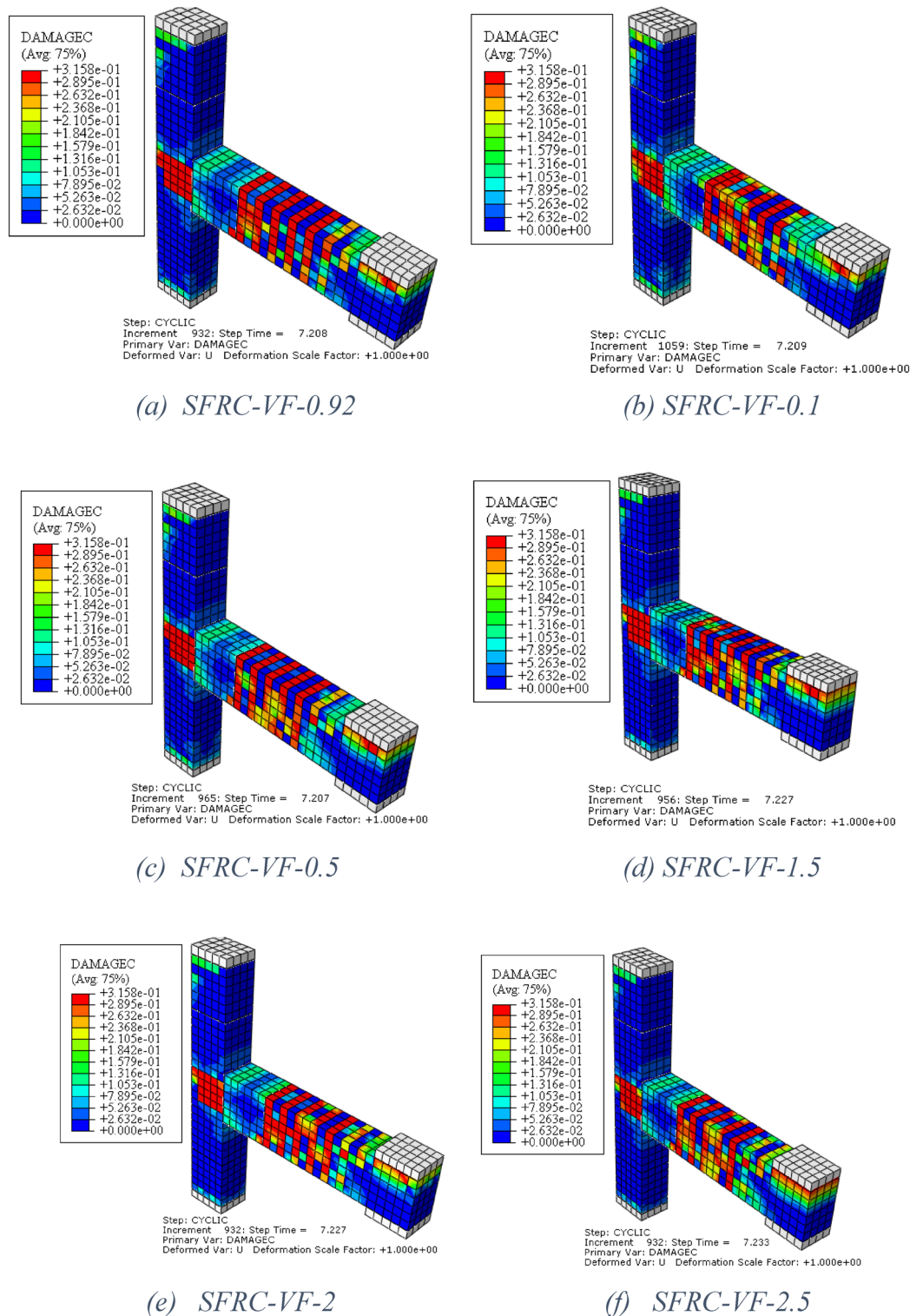


**Figure 23.** Crack patterns of the simulated specimens of VF corresponding to 2nd cycle (24 mm).

*General behavior and failure patterns of different aspect ratios*

This section investigates the behavior and failure patterns of concrete specimens with varying aspect ratios. Figure 27a and (b) provide an overview of the combined hysteresis capacity curves and facilitate comparative analysis of skeleton curves across all specimens.

**SFRC-VF-0.92 (Control).** Flexural cracks initiated at the SFRC and plain concrete junction at 12 mm deflection, with a peak load of 50.16 kN. Subsequent cycles saw crack propagation and increasing damage, resulting in

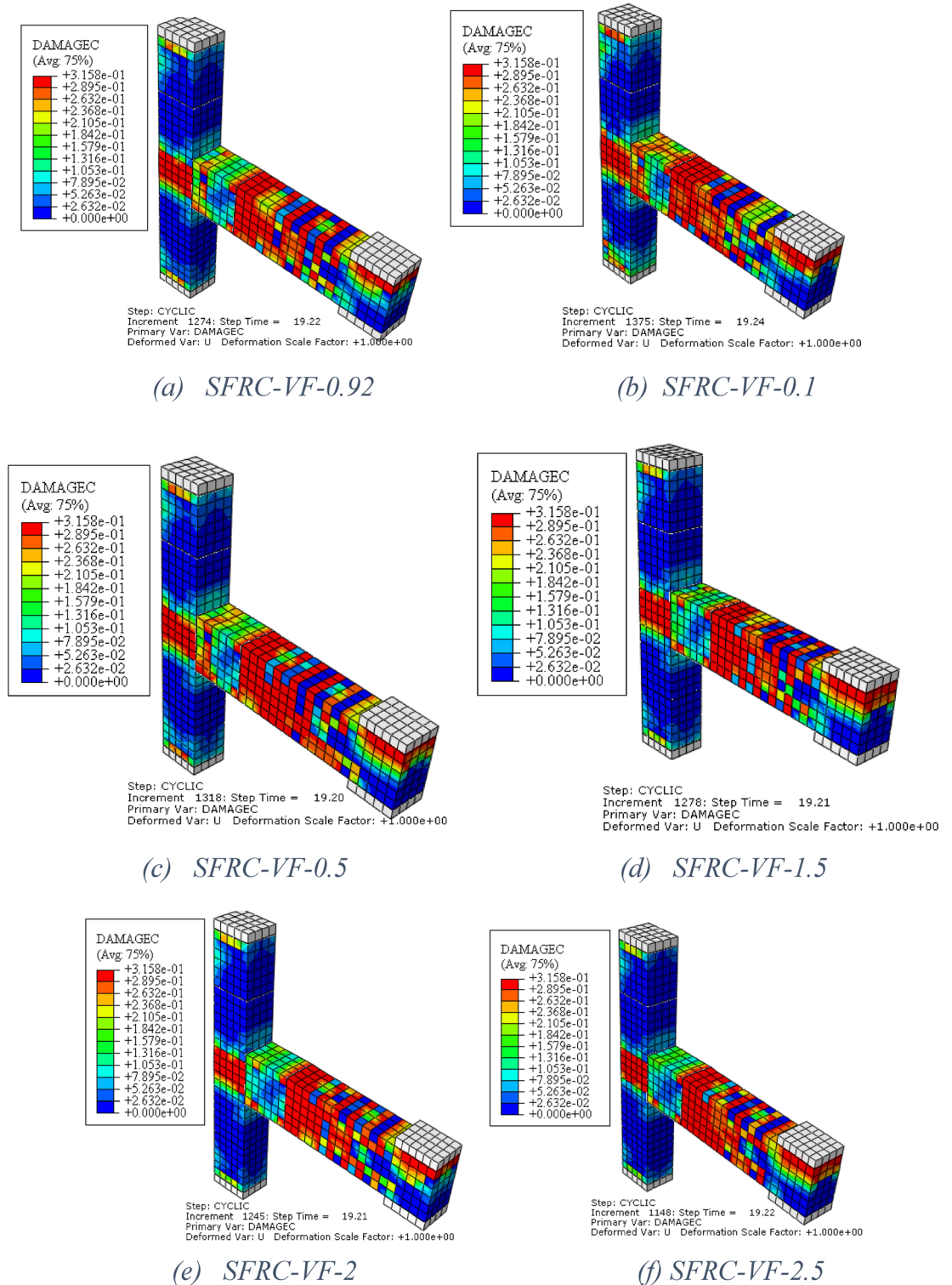


**Figure 24.** Crack patterns of the simulated specimens of VF corresponding to 3rd cycle(48 mm).

a peak load of 52.14 kN at 96 mm deflection. Failure occurred in a ductile manner, with the beam yielding before the connection (Figs. 28a, 29a, 30a and 31a).

**SFRC-AR-35.** Similar crack initiation and propagation to the control specimen. Peak load slightly lower than the control specimen (51.64 kN) at 96 mm deflection, indicating comparable behavior (Figs. 28b, 29b, 30b and 31b).

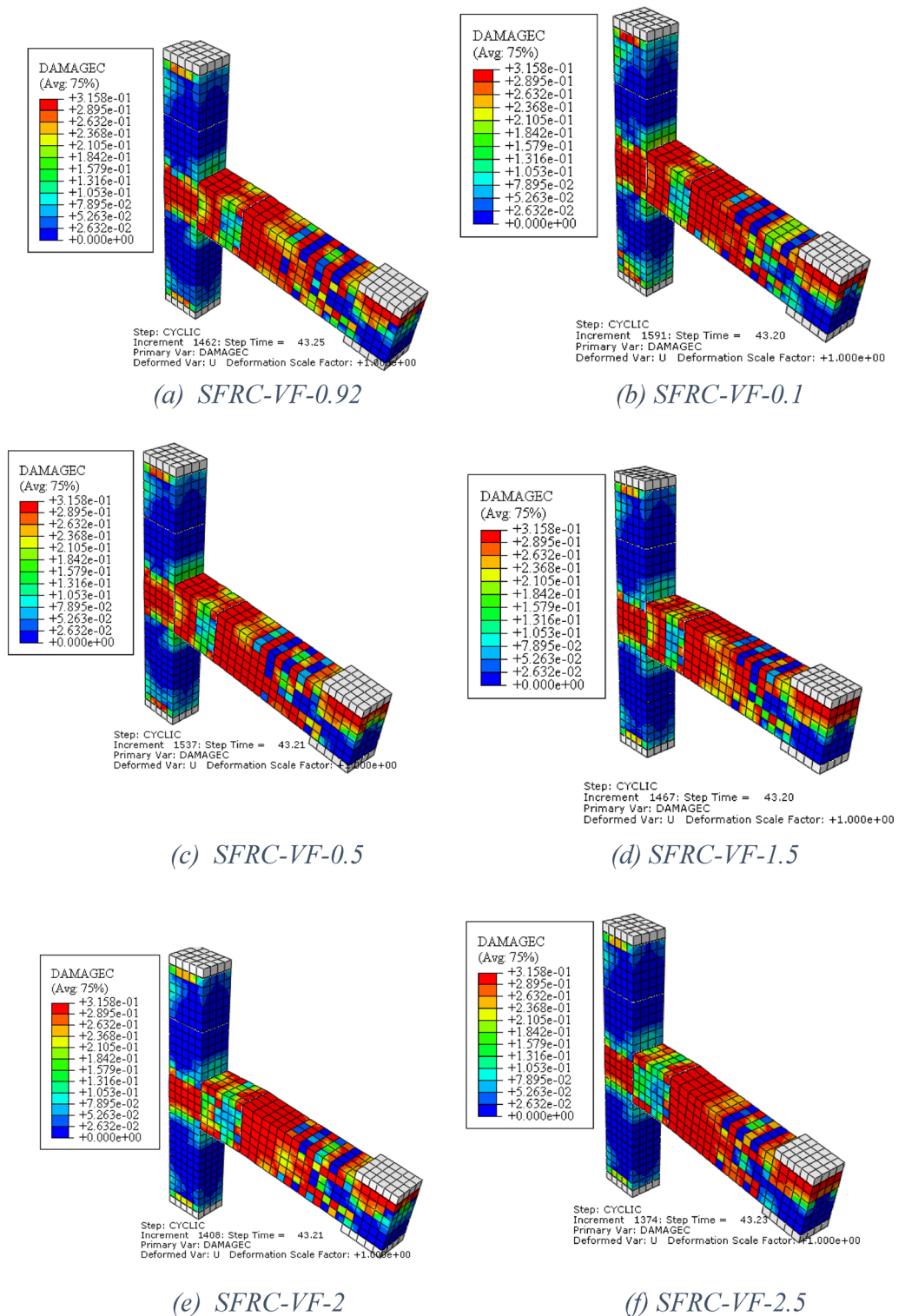


**Figure 25.** Crack patterns of the simulated specimens of VF corresponding to 4th cycle(96 mm).

**SFRC-AR-50.** Similar crack pattern and propagation, but higher maximum load capacity compared to the control model. Peak load consistently higher than the control specimen, indicating improved performance (Fig. 28c, 29c, 30c and 31c).

**SFRC-AR-75.** Crack initiation and propagation closely resemble the control specimen. Peak load significantly higher (53.89 kN) than the control specimen at 96 mm deflection, indicating enhanced load capacity (Figs. 28d, 29d, 30d and 31d).

Cycles	SFRC-VF-0.92		SFRC-VF-0.1		SFRC-VF-0.5		SFRC-VF-1.5		SFRC-VF-2		SFRC-VF-2.5	
	$\Delta$ (mm)	P (kN)	$\Delta$	P	$\Delta$	P	$\Delta$	P	$\Delta$	P	$\Delta$	P
(+ ) Cycles												
1 <sup>st</sup> Cycle	12	50.16	12	46.79	12	48.87	12	51.39	12	51.78	12	51.87
2 <sup>nd</sup> Cycle	24	56.55	24	53.65	24	55.56	24	57.23	24	56.64	24	57.74
3 <sup>rd</sup> Cycle	48	56.34	48	54.16	48	55.35	48	57.24	48	57.63	48	57.78
4 <sup>th</sup> Cycle	96	52.14	96	50.55	96	51.19	96	52.83	96	53.75	96	53.94
(- ) Cycles												
1st Cycle	-12	-54.38	-12	-51.57	-12	-53.51	-12	-55.17	-12	-55.57	-12	-54.54
2nd Cycle	-24	-57.81	-24	-55.30	-24	-55.53	-24	-58.27	-24	-58.58	-24	-58.64
3rd Cycle	-48	-55.61	-48	-53.38	-48	-53.49	-48	-55.52	-48	-57.07	-48	-57.26
4th Cycle	-96	-51.70	-96	-50.37	-96	-50.32	-96	-52.87	-96	-53.69	-96	-53.86

**Table 12.** Peak loads and their comparison of all simulated specimens (VF).

**SFRC-AR-85 and SFRC-AR-91.** Both models exhibited similar crack initiation and propagation. Peak load significantly higher than the control specimen (53.8 kN) at 96 mm deflection, indicating superior performance (Figs. 28e,f, 29e,f, 30e,f, 31e,f).

The observed increase in maximum load-taking capacity and reduction in damage near the joint core region with increasing aspect ratio aligns with previous studies. Longer and thinner steel fibers enhance the load-taking capacity by filling voids in the matrix and dissipating energy more effectively through crack bridging mechanism<sup>54,55</sup>. This mechanism delays crack initiation and propagation, increases toughness, and enhances post-cracking performance of the matrix, as demonstrated in this research.

### Stiffness degradation and energy dissipation

To assess the cyclic response of the beam-column connections, the cyclic secant stiffness was calculated for each displacement increment across the four cycles. The following equation was employed to determine the cyclic secant stiffness (K) (43).

$$K_i = \frac{P_i^+ - P_i^-}{D_i^+ - D_i^-}$$

where K represents the cyclic secant stiffness,  $P_i^+$  and  $P_i^-$  are the peak loads in the positive and negative loading directions, respectively, and  $D_i^+$  and  $D_i^-$  are the displacements corresponding to the peak loads  $P_i^+$  and  $P_i^-$ .

Figure 32 illustrates the degradation of cyclic stiffness for specimens with varying steel fiber content at each displacement increment. As observed in the figure, an increase in steel fiber content generally leads to a higher peak-to-peak stiffness. For instance, at a displacement of 12 mm, the SFRC-VF-2.5 specimen exhibited a 1.78% increase in peak-to-peak secant stiffness compared to the control specimen (SFRC-VF-0.92). Conversely, the SFRC-VF-0.1 specimen displayed a 5.90% decrease in secant stiffness compared to the control, indicating a reduction in stiffness under cyclic loading (Table 13).

Additionally, Energy dissipation for the specimens was calculated using the Hysteretic Loop Analysis Program<sup>56</sup>. Results were obtained for specimens with volume fractions of 0.1%, 0.5%, 0.92% (control specimen), 1.5%, 2%, and 2.5%. Figure 33 displays the area covered by the hysteresis loop in each cycle, which represents energy dissipation, and provides information on the cumulative energy dissipated.

The hysteresis loop area increases with displacement in each cycle, demonstrating enhanced energy dissipation. The specimen with a 2% volume fraction significantly improved energy dissipation capacity. For instance, the energy dissipation capacity of the SFRC-VF-0.1 specimen was 17,013.147 kN-mm. The SFRC-VF-1.5 and SFRC-VF-2 specimens exhibited energy dissipation capacities of 17,603.38 kN-mm and 17,898.60 kN-mm, respectively, which were higher than that of the SFRC-VF-0.1 specimen.

In particular, the incorporation of steel fibers into the joint in the SFRC-VF-2 specimen enhanced its tensile post-cracking behavior following crack development, rendering the concrete more ductile and augmenting energy dissipation. This attribute is critical for seismic design, where ductility plays a pivotal role in ensuring sufficient energy dissipation (45).

### Conclusions

This research paper focuses on the application of NLFEA to predict the behavior of RC beam-column joint considering the effect of steel fibers. The FEA modeling successfully predicts the response of SFRC beam-column connections, with an average error of less than 5%. Specimens with 0.1% and 0.5% steel fibers exhibit similar crack behavior to the control specimen, but with slightly lower load capacities (10% lower for 0.1% steel fibers and 5% lower for 0.5% steel fibers). The specimen with 2% steel fibers demonstrates crack behavior better than the control specimen and with a higher load-taking capacity (15% higher). Overall, specimens with lower volume fractions of steel fibers experience faster crack propagation and reduced load capacities, while higher volume fractions provide enhanced crack resistance and load-carrying capacity. Increased aspect ratios contribute to a 15% increase in load capacity and a 20% reduction in damage in SFRC beams near joints. This is because of

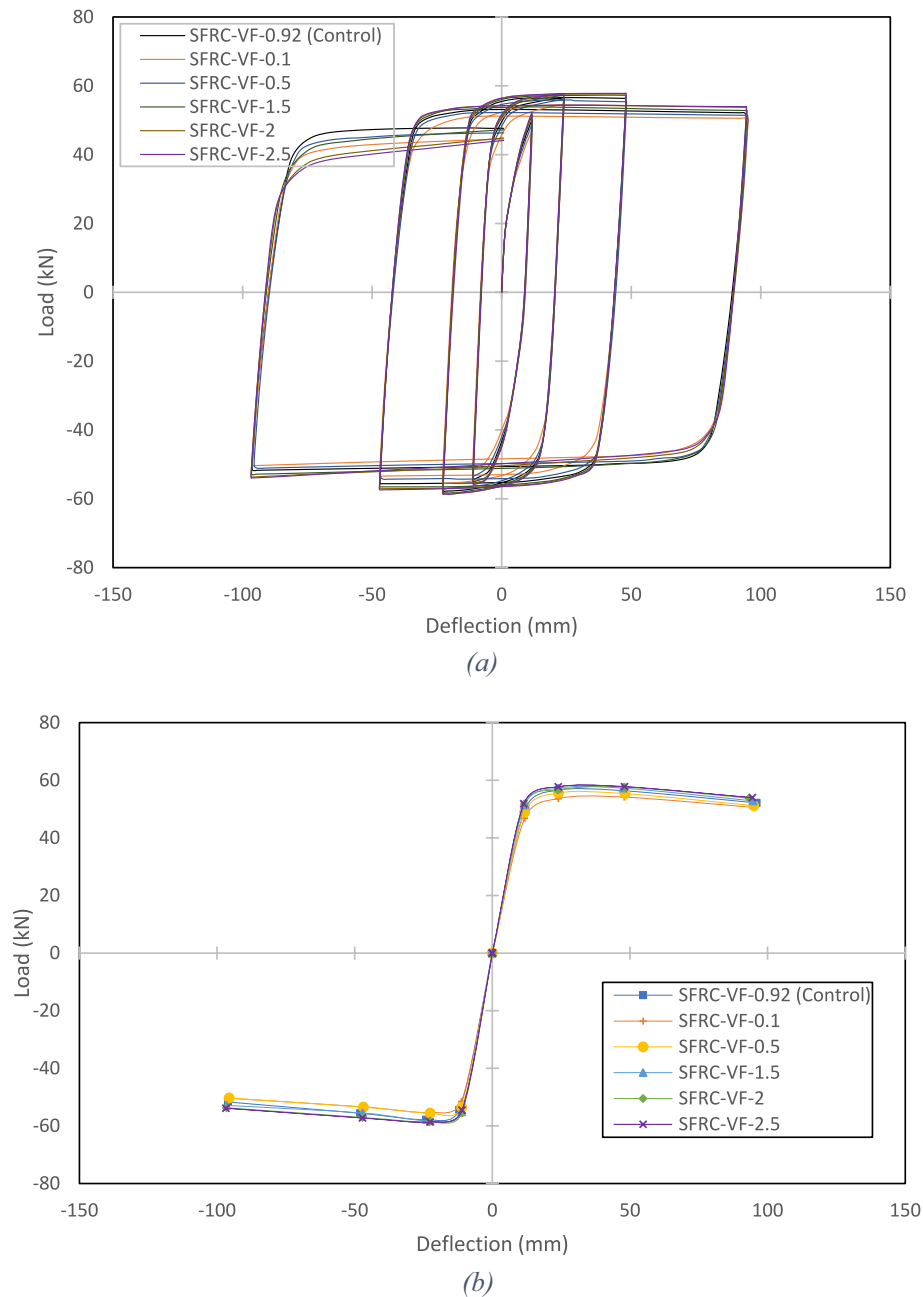


**Figure 26.** Comparison of load–deflection response (a) hysteric (b) skeleton curves.

longer, thinner steel fibers that enhance load-carrying capacity by filling voids. Steel fibers act as bridges, increasing toughness and delaying crack initiation and propagation. The effect of steel fibers on the secant stiffness is significant. Increasing the steel fiber content leads to higher peak-to-peak stiffness. Considering the damages and crack patterns, the bridging effect of steel fibers delays the formation of visible cracks by 25%, effectively limiting crack widening by 30% and minimizing concrete spalling damage by 40%. This suggests that steel fibers can be used to improve the durability and service life of SFRC beam-column joints. In conclusion, steel fibers can be used to improve the performance of SFRC beam-column joints in terms of load capacity, crack resistance, toughness, and ductility. The optimum volume fraction and aspect ratio of steel fibers depend on the specific design requirements, but a volume fraction of 2% and an aspect ratio of 60 are generally recommended for improved joint performance.

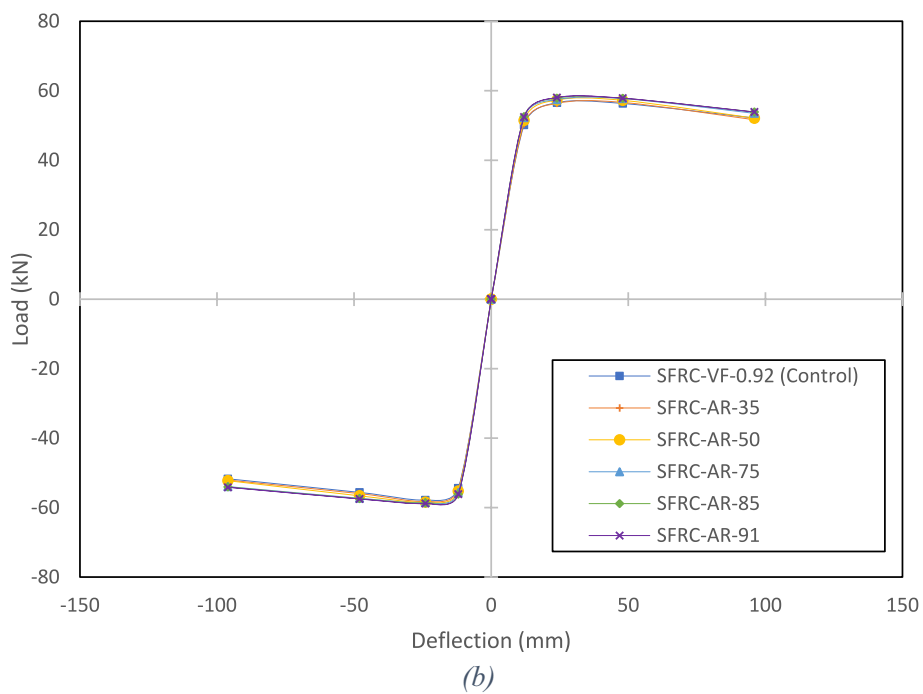
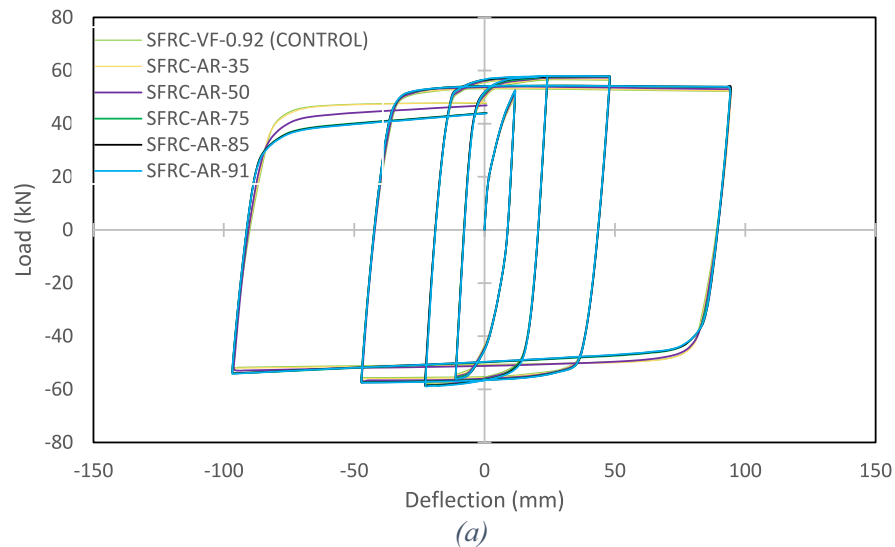
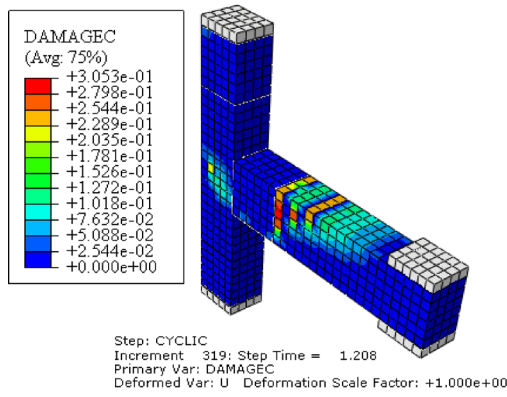
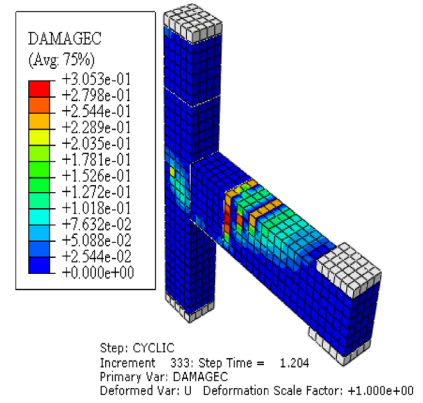


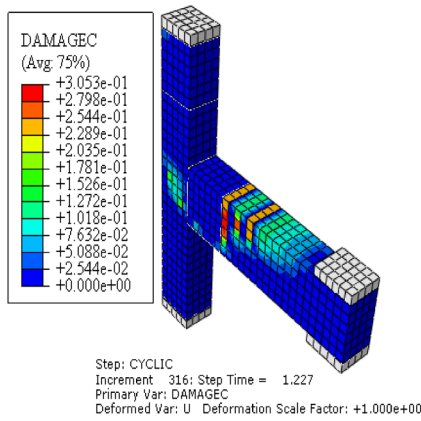
**Figure 27.** Comparison of load–deflection response (a) hysteretic (b) skeleton curves.



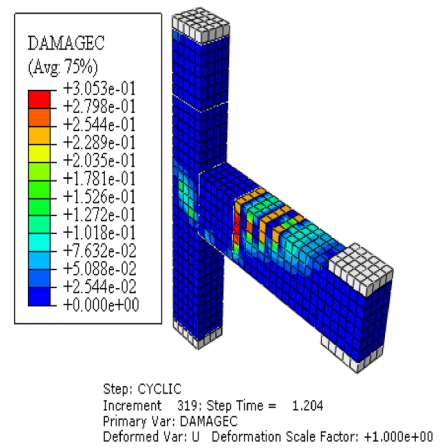
(a) SFRC-VF-0.92 (CONTROL)



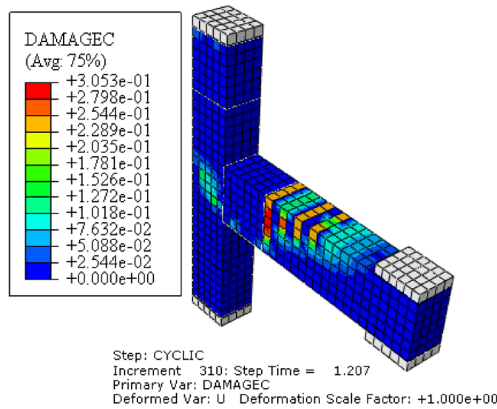
(b) SFRC-AR-35



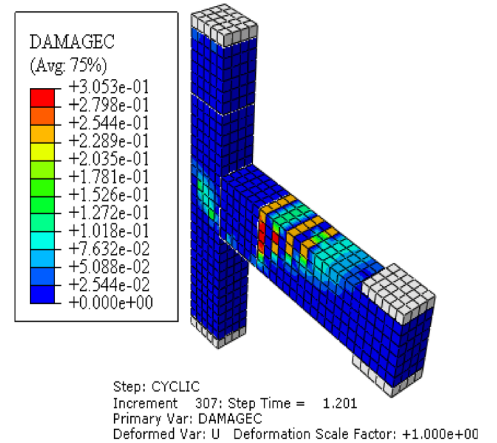
(c) SFRC-AR-50



(d) SFRC-AR-75



(e) SFRC-AR-85



(f) SFRC-AR-91

Figure 28. Crack patterns of the simulated specimens of AR corresponding to 1st cycle(12 mm).

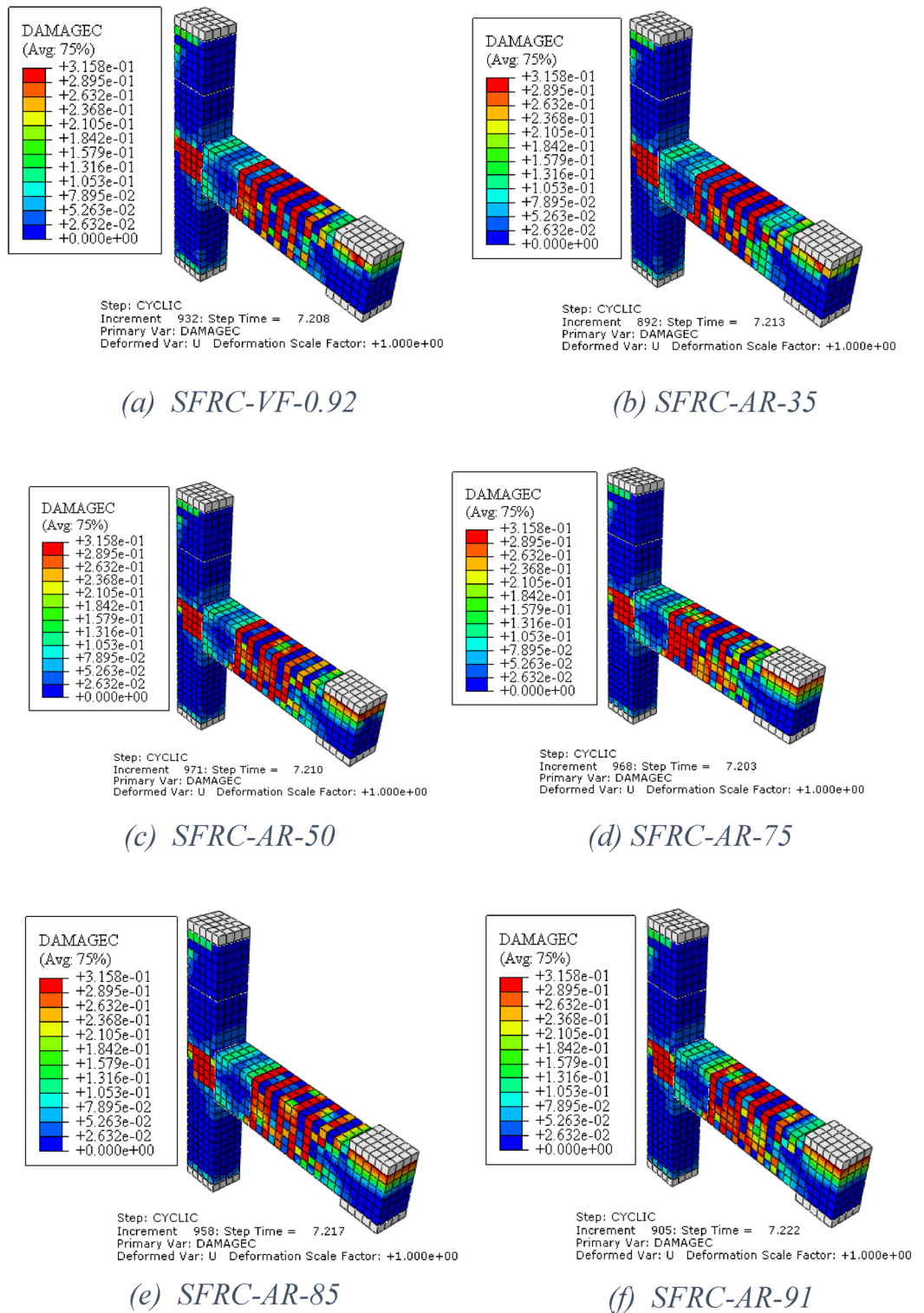


**Figure 29.** Crack patterns of the simulated specimens of AR corresponding to 2nd cycle (24 mm).

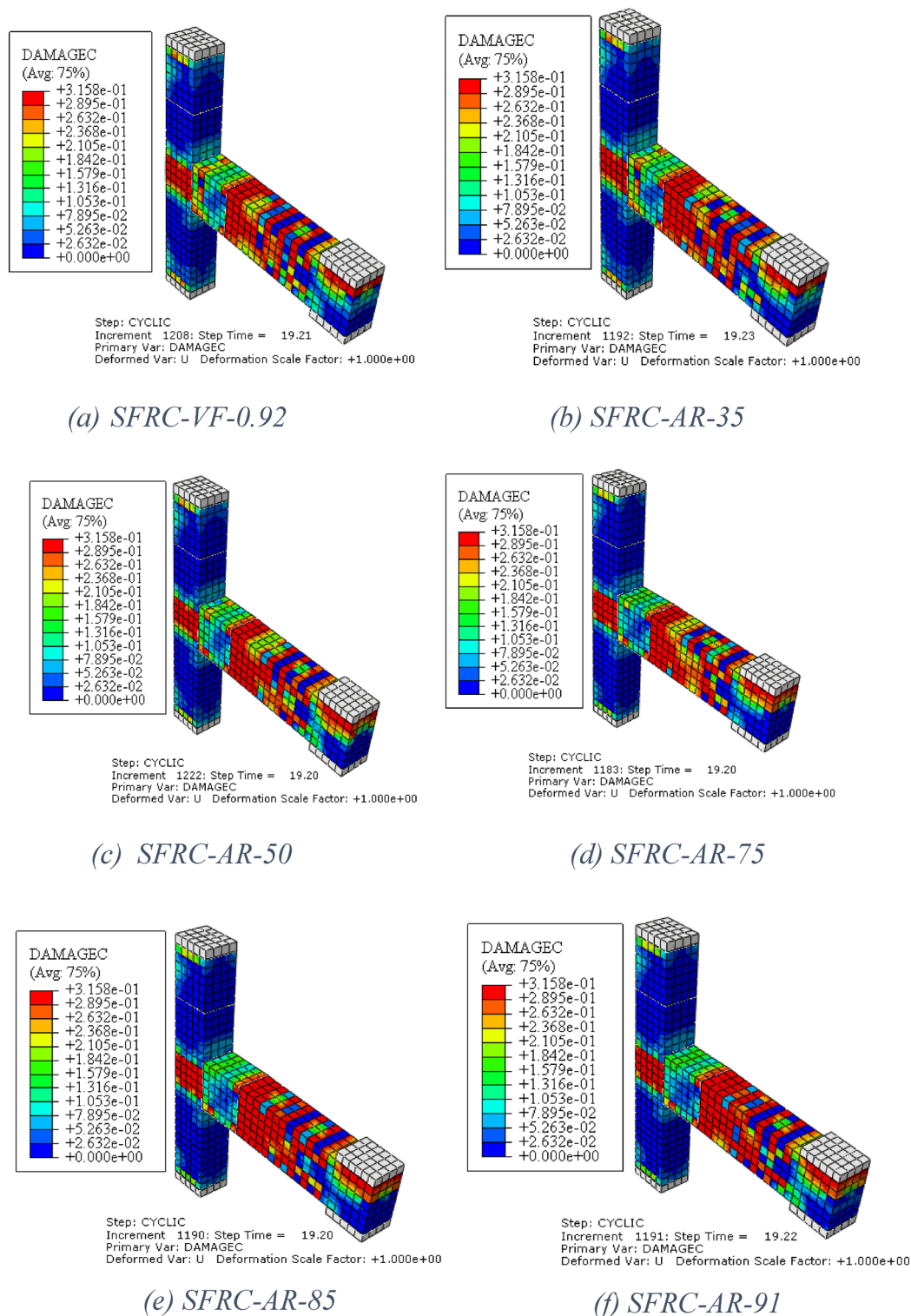
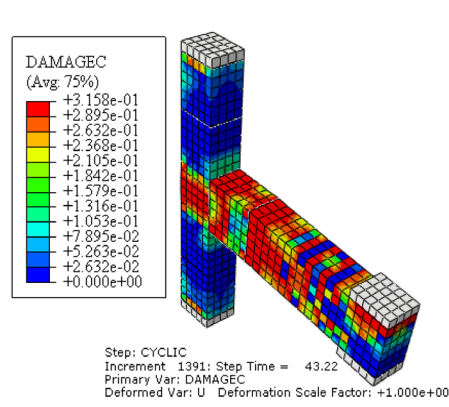
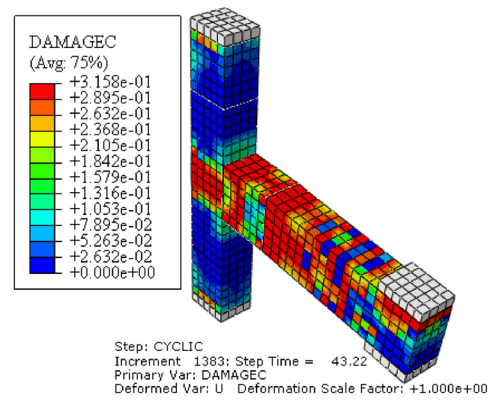


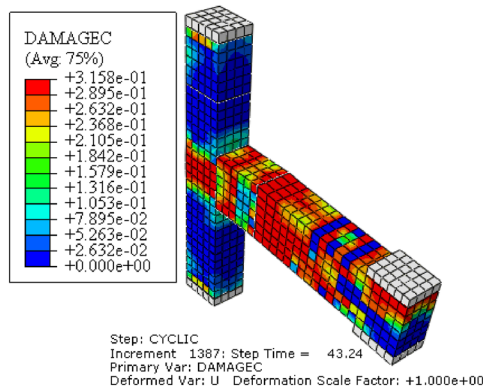
**Figure 30.** Crack patterns of the simulated specimens of AR corresponding to 3rd cycle(48 mm).



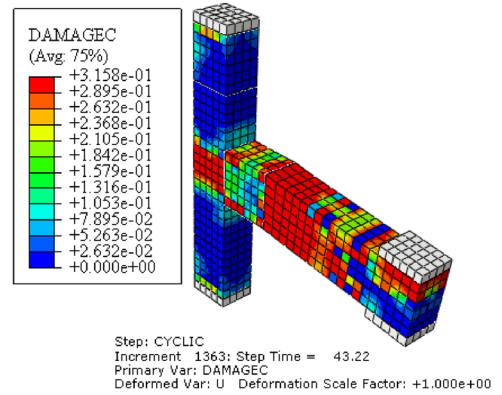
(a) SFRC-VF-0.92



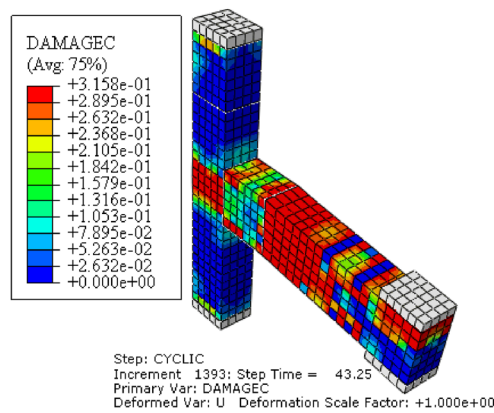
(b) SFRC-AR-35



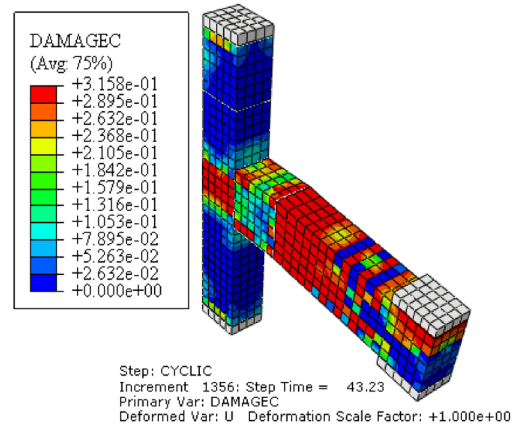
(c) SFRC-AR-50



(d) SFRC-AR-75



(e) SFRC-AR-85



(f) SFRC-AR-91

Figure 31. Crack patterns of the simulated specimens of AR corresponding to 4th cycle(96 mm).

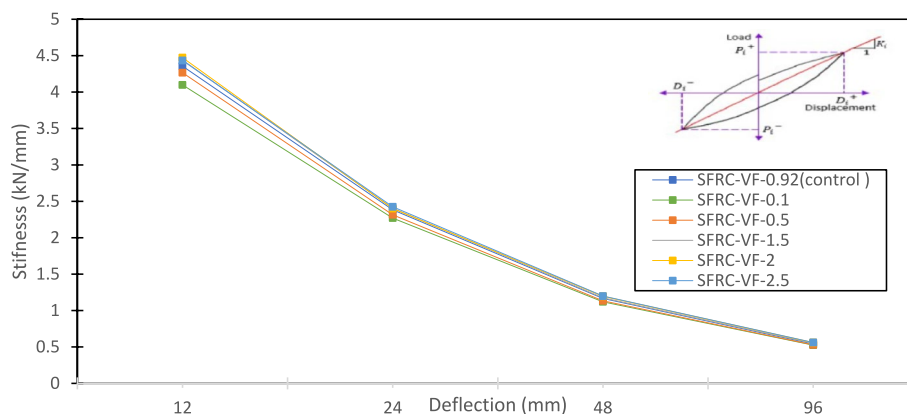


**Figure 32.** Stiffness degradation of all specimens (VF).

Cycles	VF=0.92		SFRC-AR 35		SFRC-AR 50		SFRC-AR 75		SFRC-AR 85		SFRC-AR 91	
	$\Delta$ (mm)	P(kN)	$\Delta$	P	$\Delta$	P	$\Delta$	P	$\Delta$	P	$\Delta$	P
(+ ) Cycles												
1st Cycle	12	50.16	12	50.48	12	51.47	12	52.27	12	52.54	12	52.44
2nd Cycle	24	56.55	24	56.35	24	57.31	24	57.44	24	57.84	24	58.03
3rd Cycle	48	56.34	48	56.64	48	57.23	48	57.74	48	57.82	48	57.85
4th Cycle	96	52.14	96	51.64	96	52.10	96	53.49	96	53.89	96	53.88
(- ) cycles												
1st Cycle	-12	-54.38	-12	-54.71	-12	-55.23	-12	-55.66	-12	-56.11	-12	-56.13
2nd Cycle	-24	-57.81	-24	-58.21	-24	-58.43	-24	-58.55	-24	-58.61	-24	-58.80
3rd Cycle	-48	-55.61	-48	-55.96	-48	-56.6	-48	-57.30	-48	-57.40	-48	-57.50
4th Cycle	-96	-51.70	-96	-52.06	-96	-52.24	-96	-53.94	-96	-54.02	-96	-54.14

**Table 13.** Peak loads and their comparison of all simulated specimens (AR).

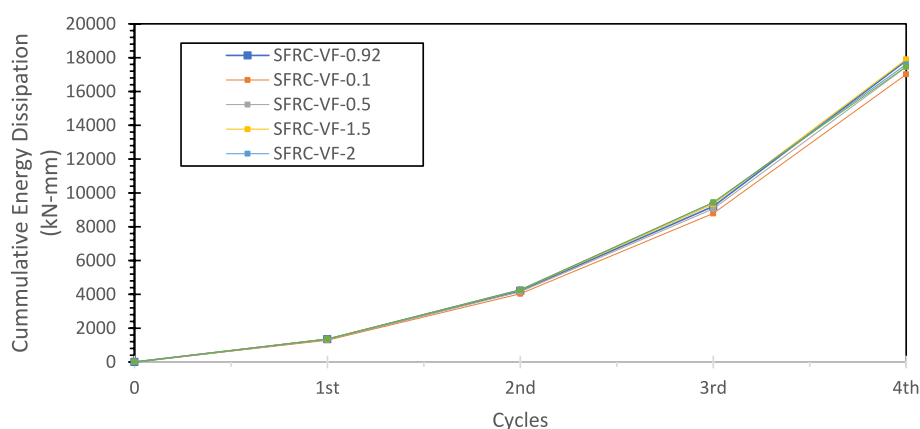


**Figure 33.** Energy Dissipation of all specimens (VF).

## Availability of data

All data used in this study is available in the manuscript.

Received: 1 January 2024; Accepted: 2 August 2024

Published online: 05 August 2024

## References

- Fayed, S., Asran, A. G. & EL-Esnawi, H. H. An experimental and numerical study on behaviour of reinforced concrete corner beam–column joint. *Innov. Infrastruct. Solut.* **8**, (2023).
- Abdel-Latif, M. A. *et al.* Effect of geometric parameters on the behavior of eccentric RC beam-column joints. *Buildings* **13**, 1980 (2023).
- He, H., Wang, S., Shen, W. & Zhang, W. The influence of pipe-jacking tunneling on deformation of existing tunnels in soft soils and the effectiveness of protection measures. *Transp. Geotech.* **42**, 101061 (2023).
- Luo, Y. *et al.* Effect of bar diameter on bond performance of helically ribbed GFRP bar to UHPC. *Elsevier Y Luo, P Liao, R Pan, J Zou, X Zhou Journal Build. Eng. 2024 Elsevier*.
- Bhavish Bhat, P. B. & Jayanth, K. Studies on the Behavior of Steel Fibre-Reinforced Concrete (SFRC) Under Monotonic Loading in Flexure: A Systematic and Simplified Finite Element Model for Assessing the Structural Performance. in *Lecture Notes in Civil Engineering* vol. 455 115–126 (Springer Science and Business Media Deutschland GmbH, 2024).
- El-Naqeeb, M. H. & Abdelwahed, B. S. Nonlinear finite element investigations on different configurations of exterior beam-column connections with different concrete strengths in column and floor. *Structures* **50**, 1809–1826 (2023).
- Shen, X., Li, B., Chen, Y. T. & Tizani, W. Experimental and numerical study on reinforced concrete beam-column joints with diagonal bars: Effects of bonding condition and diameter. *Structures* **37**, 905–918 (2022).
- Guo, M., Huang, H., Zhang, W., Xue, C. & Huang, M. Assessment of rc frame capacity subjected to a loss of corner column. *J. Struct. Eng.* **148**, (2022).
- Lu, D. *et al.* A dynamic elastoplastic model of concrete based on a modeling method with environmental factors as constitutive variables. *J. Eng. Mech.* **149**, 04023102 (2023).
- Shi, K. *et al.* Seismic performance of steel fiber reinforced high-strength concrete beam–column joints. *Materials* **14**, 4016 (2021).
- Huang, H., Li, M., Yuan, Y. & Bai, H. Experimental Research on the Seismic Performance of Precast Concrete Frame with Replaceable Artificial Controllable Plastic Hinges. *J. Struct. Eng.* **149**, (2023).
- Cui, D. *et al.* Dynamic Splitting Performance and Energy Dissipation of Fiber-Reinforced Concrete under Impact Loading. *Materials* **17**, 421 (2024).
- Abbas, A. A., Syed Mohsin, S. M. & Cotsovos, D. M. Seismic response of steel fibre reinforced concrete beam-column joints. *Eng. Struct.* **59**, 261–283 (2014).
- Pang, B. *et al.* Ultraductile waterborne epoxy-concrete composite repair material: Epoxy-fiber synergistic effect on flexural and tensile performance. *Cem. Concr. Compos.* **129**, (2022).
- Li, H., Yang, Y., Wang, X. & Tang, H. Effects of the position and chloride-induced corrosion of strand on bonding behavior between the steel strand and concrete. *Structures* **58**, (2023).
- Hamed, A. & Ghallab, A. Behavior of external beam-column connection under Earthquake loading. *Res. Hamed, AA Beah, A Ghallab researchgate.net* (2023).
- Wei, J. *et al.* Seismic performance of concrete-filled steel tubular composite columns with ultra high performance concrete plates. *Eng. Struct.* **278**, 115500 (2023).
- Fares, A. M. H. & Burak Bakir, B. Parametric study on the flexural behavior of steel fiber reinforced concrete beams utilizing nonlinear finite element analysis. *Structures* **65**, 106688 (2024).
- Jin, Z. *et al.* Internal superhydrophobic marine concrete: Interface modification based on slag microstructure regulation. *J. Build. Eng.* **86**, 108769 (2024).
- Zhou, C. *et al.* The feasibility of using ultra-high performance concrete (UHPC) to strengthen RC beams in torsion. *J. Mater. Res. Technol.* **24**, 9961–9983 (2023).
- Shan, H. *et al.* Effect of carbon dots with different sizes on chloride binding of cement. *Constr. Build. Mater.* **425**, 136103 (2024).
- Lu, D., Zhou, X., Du, X. & Wang, G. A 3D fractional elastoplastic constitutive model for concrete material. *Int. J. Solids Struct.* **165**, 160–175 (2019).
- Kim, S., Jung, H., Kim, Y. & Park, C. Effect of steel fiber volume fraction and aspect ratio type on the mechanical properties of SIFCON-based HPRFRC. *Struct. Eng. Mech.* **65**, 163–171 (2018).
- Sun, L. *et al.* Experimental investigation on the bond performance of sea sand coral concrete with FRP bar reinforcement for marine environments. *Adv. Struct. Eng.* <https://doi.org/10.1177/13694332221131153> (2022).
- Zhang, W., Liu, X., Huang, Y. & Tong, M. N. Reliability-based analysis of the flexural strength of concrete beams reinforced with hybrid BFRP and steel rebars. *Arch. Civ. Mech. Eng.* **22**, (2022).
- Yao, X. *et al.* AI-based performance prediction for 3D-printed concrete considering anisotropy and steam curing condition. *Constr. Build. Mater.* **375**, 130898 (2023).
- Almasabha, G., Murad, Y., Alghossoon, A., Saleh, E. & Tarawneh, A. Sustainability of using steel fibers in reinforced concrete deep beams without stirrups. *Sustain.* **15**, (2023).
- Huang, H., Huang, M., Zhang, W., Pospisil, S. & Wu, T. Experimental investigation on rehabilitation of corroded RC columns with BSP and HPFL under combined loadings. *J. Struct. Eng.* **146**, (2020).
- Huang, H. *et al.* Numerical investigation on the bearing capacity of RC columns strengthened by HPFL-BSP under combined loadings. *J. Build. Eng.* **39**, 102266 (2021).
- Banu, W. B., Jaya, K. P. & Vidjeapriya, R. Seismic behaviour of exterior beam-column joint using steel fibre-reinforced concrete under reverse cyclic loading. *Arab. J. Sci. Eng.* **48**, 4635–4655 (2023).
- Zhang, Z. Y., Ding, R., Nie, X. & Fan, J. S. Seismic performance of a novel interior precast concrete beam-column joint using ultra-high performance concrete. *Eng. Struct.* **222**, 111145 (2020).
- Patel, P. A., Desai, A. K. & Desai, J. A. Evaluation of RC and SFRC exterior beam-column joint under cyclic loading for reduction in lateral reinforcement of the joint region. *Mag. Concr. Res.* **65**, 405–414 (2013).
- Khalaf, N. A. & Qissab, M. A. Behavior of SFRC interior beam-column joints under cyclic loading. *Struct. Monit. Maint.* **7**, 167–193 (2020).
- Smith, P. D., Cook, W. A. & Anderson, C. A. finite element analysis of prestressed concrete reactor vessels. *Struct Eng Prestress. React Press. Vessel. H.* (1977).
- Fawaz, G. & Murcia-Delso, J. Three-dimensional finite element modeling of RC columns subjected to cyclic lateral loading. *Eng. Struct.* **239**, 112291 (2021).
- Yimer, M. A. & Aure, T. W. Numerical Investigation of reinforced concrete and steel fiber-reinforced concrete exterior beam-column joints under cyclic loading. *Iran. J. Sci. Technol. -Trans Civ. Eng.* **46**, 2249–2273 (2022).

37. Abusafaqa, F. R., Samaaneh, M. A. & Dwaikat, M. B. M. Improving ductility behavior of sway-special exterior beam-column joint using ultra-high performance fiber-reinforced concrete. *Structures* **36**, 979–996 (2022).
38. Balouch, S. U. & Forth, J. P. *Strengthening of Beam-Column Joint With Steel Fibre Reinforced Concrete During Earthquake Loading*. [https://www.academia.edu/download/48042734/Dr.\\_Sana\\_Ullah\\_Balouch\\_Postdoc\\_Report.pdf](https://www.academia.edu/download/48042734/Dr._Sana_Ullah_Balouch_Postdoc_Report.pdf) (2009).
39. Liao, L., Zhao, J., Zhang, F., Li, S. & Wang, Z. Experimental study on compressive properties of SFRC under high strain rate with different fiber content and aspect ratio. *Constr. Build. Mater.* **261**, 119906 (2020).
40. Applied Technology Council. *Interim Testing Protocols for Determining the Seismic Performance Characteristics of Structural and Nonstructural Components (FEMA 461)*. 138 (2007).
41. Mangalathu, S. & Jeon, J. S. Classification of failure mode and prediction of shear strength for reinforced concrete beam-column joints using machine learning techniques. *Eng. Struct.* **160**, 85–94 (2018).
42. Dolce, M. *et al.* 3D Dynamic tests on 2/3 scale masonry buildings retrofitted with different systems. *Proc. 14th World Conf. Earthq. Eng.* (2008).
43. Calvi, G. M., Magenes, G. & Pampanin, S. Relevance of beam-column joint damage and collapse in RC frame assessment. *J. Earthq. Eng.* **6**, 75–100 (2002).
44. Nadir, W., Ali, A. Y. & Kadhim, M. M. A. Structural behavior of hybrid reinforced concrete beam-column joints under cyclic load: State of the art review. *Case Stud. Constr. Mater.* **15**, e00707 (2021).
45. Gencoglu, M. The effects of stirrups and the extents of regions used SFRC in exterior beam-column joints. *Struct. Eng. Mech.* **27**, 223–241 (2007).
46. Ezeldin, A. S. & Balaguru, P. N. Normal- and high-strength fiber-reinforced concrete under compression. *J. Mater. Civ. Eng.* **4**, 415–429 (1992).
47. Moradi, M., Bagherieh, A. R. & Esfahani, M. R. Tensile modeling of steel fiber reinforced concrete. *Asian J. Civ. Eng.* **20**, 269–280 (2019).
48. Jankowiak, T. & LOdygowski, T. Identification of parameters of concrete. *Found. Civ. Environ. Eng.* 53–69 (2005).
49. Hussain, I., Yaqoob, M., Ehsan, A. & Rehman, S. U. Effect of viscosity parameter on numerical simulation of fire damaged concrete columns. *Civ. Eng. J.* **5**, 1841–1849 (2019).
50. Sardar, S., Mahmood, M., and Shakir, I. Nonlinear pushover analysis for steel beam-column connection. *Eurasian J. Sci. Eng.* **3**, (2017).
51. Mohamed, A. R., Shoukry, M. S. & Saeed, J. M. Prediction of the behavior of reinforced concrete deep beams with web openings using the finite element method. *Alexandria Eng. J.* **53**, 329–339 (2014).
52. Behnam, H., Kuang, J. S. & Samali, B. Parametric finite element analysis of RC wide beam-column connections. *Comput. Struct.* **205**, 28–44 (2018).
53. Shah, S. H. A. *et al.* Effect of recycled steel fibers on the mechanical strength and impact toughness of precast paving blocks. *Case Stud. Constr. Mater.* **16**, e01025 (2022).
54. Biswas, R. K. *et al.* Effects of steel fiber percentage and aspect ratios on fresh and hardened properties of ultra-high performance fiber reinforced concrete. *Appl. Mech.* **2**, 501–515 (2021).
55. Ranjbaran, F., Rezayfar, O. & Mirzababai, R. Experimental investigation of steel fiber-reinforced concrete beams under cyclic loading. *Int. J. Adv. Struct. Eng.* **10**, 49–60 (2018).
56. Mostofinejad, D. & Akhlaghi, A. Experimental investigation of the efficacy of EBROG method in seismic rehabilitation of deficient reinforced concrete beam-column joints using CFRP sheets. *J. Compos. Constr.* **21**, (2017).

## Author contributions

All authors contributed equally.

## Competing interests

The authors declare no competing interests.

## Additional information

**Correspondence** and requests for materials should be addressed to K.O. or M.F.J.

**Reprints and permissions information** is available at [www.nature.com/reprints](http://www.nature.com/reprints).

**Publisher's note** Springer Nature remains neutral with regard to jurisdictional claims in published maps and institutional affiliations.

**Open Access** This article is licensed under a Creative Commons Attribution-NonCommercial-NoDerivatives 4.0 International License, which permits any non-commercial use, sharing, distribution and reproduction in any medium or format, as long as you give appropriate credit to the original author(s) and the source, provide a link to the Creative Commons licence, and indicate if you modified the licensed material. You do not have permission under this licence to share adapted material derived from this article or parts of it. The images or other third party material in this article are included in the article's Creative Commons licence, unless indicated otherwise in a credit line to the material. If material is not included in the article's Creative Commons licence and your intended use is not permitted by statutory regulation or exceeds the permitted use, you will need to obtain permission directly from the copyright holder. To view a copy of this licence, visit <http://creativecommons.org/licenses/by-nc-nd/4.0/>.

© The Author(s) 2024, corrected publication 2024